Destructive interference of ENSO on North Pacific SST and North American precipitation associated with Aleutian low variability

Sarah M. Larson[1], Yuko Okumura[2], Katinka Bellomo[3,4], Melissa L. Breeden[5,6]

[1]Department of Marine, Earth, and Atmospheric Sciences, North Carolina State University, Raleigh, NC, USA

[2]Institute for Geophysics, University of Texas at Austin, Austin, TX, USA

[3]Department of Environment, Land and Infrastructure Engineering, Polytechnic University of Turin, Turin, Italy

[4]National Research Council of Italy, Institute of Atmospheric Sciences and Climate, Turin, Italy

[5]NOAA Physical Sciences Laboratory, Boulder, CO, USA

[6]Cooperative Institute for Research in the Environmental Sciences, University of Colorado Boulder, Boulder, CO, USA

Submitted to *Journal of Climate*

July 2021

Revised January 2022

Corresponding author: Sarah M. Larson, Department of Marine, Earth, and Atmospheric Science, North Carolina State University, 2800 Faucette Drive, 1125 Jordan Hall, Raleigh, NC, 27695, USA. E-mail: slarson@ncsu.edu

Abstract

Identifying the origins of wintertime climate variations in the Northern Hemisphere requires careful attribution of the role of El Niño - Southern Oscillation (ENSO). For example, Aleutian low variability arises from internal atmospheric dynamics and is remotely forced mainly via ENSO. How ENSO modifies the local sea surface temperature (SST) and North American precipitation responses to Aleutian low variability remains unclear, as teasing out the ENSO signal is difficult. This study utilizes carefully designed coupled model experiments to address this issue. In the absence of ENSO, a deeper Aleutian low drives a positive Pacific Decadal Oscillation (PDO)-like SST response. However, unlike the observed PDO pattern, a coherent zonal band of turbulent heat flux-driven warm SST anomalies develops throughout the subtropical North Pacific. Furthermore, non-ENSO Aleutian low variability is associated with a large-scale atmospheric circulation pattern confined over the North Pacific and North America and dry precipitation anomalies across the southeast United States. When ENSO is included in the forcing of Aleutian low variability in the experiments, the ENSO teleconnection modulates the turbulent heat fluxes and damps the subtropical SST anomalies induced by non-ENSO Aleutian low variability. Inclusion of ENSO forcing results in wet precipitation anomalies across the southeast United States, unlike when the Aleutian low is driven by non-ENSO sources. Hence, we find that the ENSO teleconnection acts to destructively interfere with the subtropical North Pacific SST and southeast United States precipitation signals associated with non-ENSO Aleutian low variability.

1. Introduction

Large-scale atmospheric circulation variability and the associated SST patterns are an important source of predictability for terrestrial climate anomalies over North America (e.g., Ropelewski and Halpert 1989; Latif and Barnett 1996; Dai et al. 1998; Trenberth et al. 1998; Hoerling and Kumar 2002; Di Lorenzo and Mantua 2016; Newman et al. 2016). A prevalent weather regime is associated with the Aleutian low and is characterized by the waxing and waning in strength of the climatological low pressure center over the North Pacific. Variations in Aleutian low strength are known to impact a wide range of earth system components, including ocean temperature, marine ecosystems, and precipitation (e.g., Trenberth and Hurrell 1994; Mantua et al. 1997; Cayan et al. 1998; Di Lorenzo and Ohman 2013). The Aleutian low is also the most prominent surface feature of the Pacific-North American Pattern (PNA; Wallace and Gutzler 1981a), a large-scale atmospheric circulation pattern that connects the subtropics and midlatitudes across the Pacific and North America. Given that PNA and Aleutian low time series are highly correlated (Trenberth and Hurrell 1994), we focus on the Aleutian low in this study.

Aleutian low variability, often as part of the PNA pattern, arises from both internal atmospheric dynamics and remote forcing mainly via El Niño – Southern Oscillation, or ENSO (e.g., Trenberth and Hurrell 1994; Lau 1997). For example, chaotic atmospheric variability may result in an anomalously strong Aleutian low that persists through the winter. Alternatively, ENSO is well known to modulate Aleutian low strength, as part of a large-scale pattern that is similar to the PNA but shows a more zonally symmetric pattern (Livezey and Mo 1987; Trenberth et al. 1998; Hoerling and Kumar 2002; Straus and Shukla 2002; Johnson and Feldstein 2010; Li et al. 2019). For example, the atmospheric Rossby wave response to suppressed convection in the tropical Pacific associated with La Niña events, the cold phase of ENSO, is notorious for weakening the wintertime Aleutian low (Blackmon et al. 1983; Trenberth and Hurrell 1994) and driving anomalous ridging across the central United States (e.g., Trenberth et al. 1998). The resulting alterations in the atmospheric circulation are associated with a northward shift of the storm track and anomalously dry conditions over the southern states (e.g., Ropelewski and Halpert 1989; Dai et al. 1998). ENSO's modulation of Aleutian low strength also impacts turbulent heat flux anomalies (hereafter, Q'_{turb}) and anomalous Ekman transports over the North Pacific (Alexander 1992; Alexander et al. 2002; Alexander and Scott 2008), driving SST variability resembling the Pacific Decadal Oscillation (PDO; Namias et al. 1988) pattern, thereby completing the "atmospheric bridge" (Lau and Nath 1994). Forcing from thermodynamically coupled modes and other tropical basins, may also drive fluctuations in the Aleutian low (e.g., Hoerling and Kumar 2002; Deser and Phillips 2006; Okumura et al. 2009; Clement et al. 2011).

Aleutian low variability arising from a combination of internal dynamics and ENSO typically forces a large-scale PDO-like pattern. This SST anomaly pattern emerges as the leading mode of North Pacific SST variability that is pronounced on decadal timescales. The positive phase of the PDO is characterized by warm SST anomalies along the U. S. west coast and cold SST anomalies extending from the western North Pacific into the interior basin through the Kuroshio Extension region (Mantua et al. 1997). The PDO pattern is generated primarily through the modulation of Q'_{turb} and anomalous wind stress forcing on the ocean surface (Alexander 1992; Miller et al. 1994). The ocean dynamical response to wind stress variability plays an important role in PDO variability, particularly in elongating the timescale of PDO variations through ocean adjustment via midlatitude ocean Rossby waves (Miller et al. 1998; Deser et al. 1999; Schneider and Miller 2001; Seager et al. 2001; Kwon and Deser 2007), Ekman transports

(Schneider et al. 2002; Alexander 2010), Kuroshio-Oyashio current variability (Miller and Schneider 2000; Seager et al. 2001; Schneider et al. 2002; Qiu 2003; Schneider and Cornuelle 2005), and the “reemergence” mechanism (Alexander and Deser 1995; Alexander et al. 1999).

Many observational and modeling studies identify linkages between ENSO and PDO phases. Trenberth (1990) shows that a deeper Aleutian low and a positive PDO coincided with multiple El Niño events and lack of La Niña events during 1977-1988. A similar relationship between ENSO and PDO is found in observations and climate model simulations (Kiem et al. 2003; Vimont 2005; Verdon and Franks 2006; Okumura et al. 2017; Sun and Okumura 2020; Power et al. 2021). Studies also argue that the relative phasing of ENSO and PDO result in a constructive or destructive interference of the resulting teleconnection patterns over North America (Gershunov and Barnett 1998; McCabe and Dettinger 1999; Cole et al. 2002; Brown and Comrie 2004; Hu and Huang 2009; Wang et al. 2012). Therefore, identifying the origins of Northern Hemisphere climate anomalies requires careful attribution of the role of ENSO.

Although it is well known that interannual variations associated with ENSO are an important contributor to lower frequency PDO-like SST anomalies (Newman et al. 2003; Schneider and Cornuelle 2005; Vimont 2005), how ENSO modifies the North Pacific SST and North American precipitation responses to Aleutian low variability each winter season remains unclear. We note prior studies argue difficulty in using the PDO to predict seasonal North American impacts (Kumar et al. 2013; Kumar and Wang 2015), which is another motivator for us to instead focus on the role of ENSO forcing. Furthermore, it is unclear whether the short observational record is sufficient to accurately characterize PDO impacts in nature (McAfee 2014). In the presented analyses, we only consider the PDO-like pattern as a typical SST response to Aleutian low variability, although we discuss implications for the PDO more broadly in the final discussion.

This study aims to closely examine North Pacific SST and North American precipitation signals associated with Aleutian low variability originating from ENSO versus non-ENSO sources. We utilize a novel set of coupled model experiments to analyze these contributions separately. The paper is organized as follows. Section 2 introduces the coupled model experiments and observationally-based datasets. Validation of the model experiments is presented in Section 3 and the general methods for analyses are in Section 4. Section 5 contains the results, including the SST and precipitation signals associated with Aleutian low variability in each experiment. Section 6 provides a summary and discussion.

2. Coupled model experiments and observationally-based datasets

All model experiments are performed with a nominal 1° horizontal resolution version of the National Center for Atmospheric Research (NCAR) Community Earth System Model version 1.2.0 (Hurrell et al. 2013) with present-day (year 2000) forcing. The ocean model is the Parallel Ocean Program version 2 (POP2; Smith et al. 2010). The atmosphere model is the Community Atmosphere Model version 4 (CAM4; Neale et al. 2013), therefore this version is more closely aligned with the NCAR Community Climate System Model version 4 (CCSM4; Gent et al. 2011) but with the updated diabatic processes parameterizations of CAM5 (Hurrell et al. 2013). For clarity, this version of the model will be referred to as CESM1-CAM4 but a brief description of CCSM4's fidelity in simulating Pacific climate variability is provided. Note that the characteristics described are for a pre-industrial version of the model with year 1850 radiative forcing, whereas a present-day version with year 2000 forcing is used in this study. According to

Deser et al. (2012), CCSM4 simulates realistic spatial patterns and timescales of ENSO SST and decadal North Pacific SST variability. The amplitude of ENSO variability is roughly 30% stronger in CCSM4 compared to HadISST and the periodicity is more confined to the 3-6-yr range compared to the broader spectral peak in observations. Impacts of this caveat are mentioned where appropriate. Wintertime modulation of the Aleutian low via ENSO teleconnections is realistic, although the anomalies tend to persist too long into spring (Deser et al. 2012). The spatial pattern of decadal North Pacific SST variability in CCSM4 includes a tropical SST signature although it is slightly weaker than in observations. Overall, this model is deemed suitable for the task at hand.

In this study, we carry out CESM1-CAM4 model experiments with varying degrees of coupled air-sea processes resolved as explained in the following subsections. While some studies argue that the atmospheric response to ENSO does not require interactive ocean dynamics (Jha and Kumar 2009), we aim to also investigate the SST response to ENSO and non-ENSO driven Aleutian low variations. We adopt a model framework that minimizes potential air-sea heat flux biases related to prescribed SST experiments (Saravanan and Chang 1999; Yulaeva et al. 2001; Sutton and Mathieu 2002) and allows for the examination of both the ocean response and atmospheric variables related to Aleutian low variability. Table 1 summarizes each model experiment and lists the physical processes that drive Aleutian low variability and the associated SST anomaly response in each experiment. Each experiment is 300 years in length and subject to present-day (year 2000) radiative forcing.

a. Mechanically decoupled (MD) experiment

CESM1-CAM4 is first integrated in a mechanically decoupled (MD) configuration to simulate climate variability due to anomalous buoyancy (thermal + freshwater flux) coupling alone (Larson and Kirtman 2015; Larson et al. 2017, 2018b, 2020). The experiment is implemented by forcing the ocean component of the model with CESM1-CAM4 seasonally-varying monthly wind stress climatology, interpolated to daily values. The wind stress climatology is computed from a fully coupled version of the model introduced below. Importantly, the framework does not thermodynamically decouple the air-sea: wind variability is applied to the bulk formula for Q'_{turb}. This allows for consistent air-sea thermal fluxes between the atmosphere and ocean. By definition, this experiment lacks interannual ENSO variability characterized by large thermocline displacements, as anomalous wind stress coupling in the equatorial Pacific is necessary to simulate ENSO variability through inclusion of an active Bjerknes feedback (Larson and Kirtman 2015). It follows that in the MD, SST anomalies linked to Aleutian low variability, by definition, can only be forced via extratropical air-sea heat fluxes that are unrelated to ENSO (see Table 1). The MD differs from a slab ocean coupled model, which also lacks canonical ENSO variability, as the MD includes a dynamical ocean model with seasonally varying mean ocean circulation, seasonally varying mixed layer depth, and anomalous buoyancy-driven ocean dynamics (Larson et al. 2020). Both slab and MD model versions have been shown to generate thermodynamically coupled SST variability in the ENSO region (e.g., Dommenget 2010; Clement et al. 2011; Larson et al. 2018b), but the MD SST can be influenced by the mean ocean circulation and buoyancy induced variability.

b. Mechanically decoupled equatorial Pacific (MD_{EqPac}) experiment

Next, CESM1-CAM4 is integrated with only the equatorial Pacific mechanically decoupled from anomalous wind stress, hereafter the MD_{EqPac}. Elsewhere, the model is fully coupled in terms of both anomalous buoyancy and momentum fluxes. The same prescribed wind stress climatology is used as in the MD, except only in the tropical Pacific. Like the MD, MD_{EqPac} does not simulate ENSO variability. Different from the MD, the SST anomaly response to Aleutian low variability in the MD_{EqPac} can be generated via anomalous heat flux *and* wind stress driven ocean processes, including anomalous wind stress driven Ekman transports, except those related to ENSO.

To implement this framework, between 5°S-5°N, the Pacific Ocean is forced with the model's wind stress climatology. From 5°S-7°S and 5°N-7°N, the ocean is forced with climatology plus 25% of the wind stress anomaly generated by the atmosphere. The fraction of the wind stress anomalies allowed to force the ocean increases to 50% from 7°S-9°S and 7°N-9°N, 75% from 9°S-11°S and 9°N-11°N, and everywhere else the full wind stress anomaly generated by the atmosphere model forces the ocean. Tapering the anomaly forcing in this way reduces the possibility that an erroneous anomalous wind stress curl is generated by the imposed climatological wind stress forcing. Contrasting the MD_{EqPac} with the MD experiment reveals the impact of non-ENSO, anomalous wind stress-driven ocean dynamics in driving the SST response to Aleutian low variability.

c. Fully Coupled (FC) experiment

The FC experiment is the fully coupled version of CESM1-CAM4. This version includes both anomalous buoyancy and momentum coupling globally, the latter of which enables ENSO variability. SST anomalies linked to Aleutian low variability are forced via air-sea heat fluxes *and* anomalous wind stress driven ocean dynamics that are either driven via internal atmospheric variability unrelated to ENSO or remotely via tropical forcing. Therefore, contrasting FC with the MD_{EqPac} experiment indicates the fraction of climate variability driven by or associated with ENSO and the associated teleconnections.

d. Observationally-based datasets

Several observationally-based fields are analyzed to compare to the model. The Hadley Center Sea Ice and SST (HadISST) dataset is used for observed SST (Rayner et al. 2003). HadISST is on a 1° horizontal global grid. When comparing to the mean state SST in the model, years 1980-2020 of HadISST are selected to closely encompass the "present-day" time period. Sea level pressure, 500 hPa geopotential height, 200 hPa winds, sensible heat flux, and latent heat flux are used from both the National Center for Environmental Prediction / National Center for Atmospheric Research (NCEP/NCAR) reanalysis from 1948-2020 (Kalnay et al. 1996) and the European Centre for Medium Range Weather Forecasting Re-Analysis (ERA5; (Hersbach et al. 2020) from 1979-2019. NCEP/NCAR reanalysis data is provided on a 2.5° horizontal grid and ERA5 reanalysis is on a 0.25° horizontal grid. The time period of the HadISST dataset is modified to match the time period of the reanalysis products, respectively, when appropriate. The precipitation datasets used are the NOAA PRECipitation REConstruction dataset provided on a 2.5° horizontal grid from 1948-2020 (Chen et al. 2002) and Version 2 of the Global Precipitation Climatology Project (GPCP; Adler et al. 2003) from 1979-2020.

3. Experiment validation

a. SST climatology and variability

Fig. 1 shows the annual mean SST climatology for the model experiments and HadISST. In general, the model experiments show no dramatic difference in the mean SST (Fig. 1a-c), confirming the experimental setup does not substantially impact the mean state. The model is slightly warmer in the cold tongue region and the meridional SST gradient in the North Pacific is slightly weaker than HadISST (Fig. 1d; see also Larson et al. 2017).

Comparing the three experiments, only the FC shows substantial SST variability in the tropical Pacific (Fig. 1a-c; shading), confirming that both MD and MD_{EqPac} generally lack ENSO variability. The MD experiment shows lower variance nearly everywhere compared to MD_{EqPac}, FC, and HadISST, as primarily only anomalous heat fluxes drive SST variability in MD. This is expected, as anomalous wind stress coupling drives considerable SST anomaly variance in the western boundary current regions and regions where vertical ocean dynamics are important (e.g., Larson et al. 2018b). The variance in the western boundary current regions is comparable between MD_{EqPac} and FC, as expected given that both experiments are fully coupled in the extratropics. However, the SST variance is slightly higher in the Kuroshio Extension and lower in the Gulf Stream Extension compared to observations. The variance in the interior basin of the North Pacific compares well with observations, albeit the observed variance is likely underestimated given the short time period over which the variance is computed. Finally, compared to observations, the FC experiment shows higher SST variance in the central equatorial Pacific and the cold tongue extends too far west, both of which are known biases in CCSM4 (Deser et al. 2012).

b. Tropical Pacific SST variability

To confirm the removal of canonical ENSO variability in MD and MD_{EqPac}, Fig. 2 shows the time series of the Niño-3.4 SST anomaly index and the associated power spectrum for each experiment. The Niño-3.4 index is defined as the area-averaged SST anomaly over 5°S-5°N, 170°W-120°W. Fig. 2 confirms that canonical ENSO variability is removed as evidenced by the lack of Niño-3.4 variability in the MD and MD_{EqPac} time series (Fig. 2a) and the lack of variance at interannual timescales in the power spectra (Fig. 2b). The standard deviation of the Niño-3.4 index for the MD, MD_{EqPac}, and FC experiments over the full 300-yr period are 0.09, 0.16, and 0.96°C, respectively. Comparing the standard deviations of MD and FC suggests that a small fraction of the Niño-3.4 variability in the FC is driven by anomalous thermal fluxes in this model. Larson et al. (2018a) demonstrate that the source of this variability is the Q'_{turb} associated with the South Pacific Meridional Mode (SPMM; Zhang et al. 2014). Another small fraction of the Niño-3.4 variability in the FC is linked to anomalous wind stress driven ocean dynamics (hereafter, τ'-dynamics) originating outside the equatorial Pacific, as implied by comparing the standard deviation of Niño-3.4 in the MD_{EqPac} and MD. This is likely related to the "trade wind charging" (TWC) mechanism (Anderson and Perez 2015). According to the TWC paradigm, anomalous wind stress curl in the extratropical North Pacific drives an equatorward Sverdrup transport, thereby increasing the oceanic heat content in the west-central equatorial Pacific. The heat content anomaly then propagates eastward along the thermocline and emerges as SST anomaly warming in the eastern Pacific, priming the system for El Niño. In the presence of an active Bjerknes feedback, the TWC-generated SST anomaly grows into a moderate El Niño (Chakravorty et al. 2020). However, this additional growth is unsupported in the MD_{EqPac}.

When the Bjerknes feedback is active (e.g., FC), the power spectrum shows more variance at decadal frequencies (Fig. 2b). After applying an 8-yr low-pass Lanczos filter to the

Niño-3.4 index of each experiment, the standard deviation of the tropical Pacific decadal variability in the MD, MD_{EqPac}, and FC experiments are roughly 0.05, 0.1, and 0.22°C, respectively. This suggests that a substantial portion of the decadal Niño-3.4 variability in the model is not related to decadal variations in canonical ENSO variability. Further investigation of the origin of this decadal signal may be related to thermally coupled processes (e.g., Clement et al. 2011), but is beyond the scope of the present analysis.

4. Methods

We are interested in the SST and precipitation patterns associated with variations in Aleutian low strength that persist throughout the winter. To isolate these timescales, we first average all monthly anomalies over boreal winter months from November to March, or NDJFM (hereafter, referred to as "wintertime") averages, when Aleutian low variability peaks. Anomalies are computed by removing the monthly mean climatology in the model experiments. In observations, anomalies are calculated by linearly detrending the time series at each grid point and then removing the monthly climatology. Analyses were repeated for December-February (DJF) and January-March (JFM) averages. All major conclusions are insensitive to whether analyses are applied over DJF, JFM, or the full NDJFM, although anomalies are typically stronger for the 3-mo averages. We choose to show the NDJFM anomalies to highlight persistent anomalies over the extended season.

Aleutian low variability is estimated using the North Pacific Index (NPI), defined as the area-averaged sea level pressure anomalies over 30°N-65°N, 160°E-140°W (Trenberth and Hurrell 1994). The standard deviation of the wintertime NPI for the MD, MD_{EqPac}, and FC experiments are approximately 3.0, 3.2, and 3.5 hPa, respectively. The models overestimate the variability in the reanalysis products, with ERA5 and NCEP/NCAR reanalysis standard deviations near 2.5 and 2.2 hPa, respectively. Visual inspection of the wintertime NPI power spectra for the FC experiment and reanalysis products shows that the most discrepancy is at interannual and decadal timescales (Fig. 3a). At timescales of 3-5 years, this discrepancy is likely linked to the model's overly strong ENSO variance (Deser et al. 2012). When ENSO forcing is removed as in MD_{EqPac}, the power spectra at 3-5-yr timescales compares more closely to the reanalyses. At timescales of < 2-3 years, even the MD and MD_{EqPac} overestimate the variance. The large variance suggests the model generates too much year-to-year Aleutian low variability generated via internal atmospheric dynamics or tropically induced variations from other basins, as both the MD and MD_{EqPac} retain a portion of the precipitation variance in the tropical Indian and Atlantic Oceans seen in the FC (Fig. 4). While this is a caveat to our analysis, we note that all major results are reproducible even after applying a 3-year Lanczos filter (to remove the overly high variance, high frequencies) to the NPI indices prior to comparison of the experiments. If the NPI time series is standardized prior to computing the spectra (Fig. 3b), variability is similarly distributed across timescales for all time series, except the FC overestimates variability around 4 years likely due to the overly strong ENSO in this model.

The wintertime-averaged NPI time series are used to categorize anomalous Aleutian low years. To compare the experiments, the threshold for anomalously strong (–NPI) or weak (+NPI) wintertime Aleutian low years is defined relative to the standard deviation of the wintertime NPI from FC (+/– 3.5 hPa). All wintertime averages that meet or exceed 3.5 hPa qualify as +NPI events and all that are less than or equal to –3.5 hPa are –NPI events. This way, similar amplitude events are counted similarly for each model experiment (see Table 2 for event count). To reflect a positive PDO-like SST anomaly response, composites are shown as [–NPI - (+NPI)]

/ 2, as a +PDO-like SST is associated with a deepened Aleutian low (e.g., –NPI). The composite differences show the component of the response that is linear with respect to sign of the NPI. Generally, the spatial patterns are similar for both +NPI and –NPI in this model (not shown). Significant differences in anomaly composites between the experiments are evaluated using a two-sided Welch's t-test, which does not assume the variances of the two samples are the same. Where the variances are the same, the Welch's t-test performs similarly to the Student's t-test.

5. Results

a. The SST anomaly response to Aleutian low variability

Fig. 5 depicts the SST and SLP anomalies associated with a deepened Aleutian low in each experiment. Aleutian low variability driven by non-ENSO sources (e.g., MD and MD_{EqPac}) generates a North Pacific SST anomaly pattern that resembles the PDO pattern but is confined to the North Pacific (Fig. 5a-b). The emergence of a PDO-like SST response in the MD (Fig. 5a), which lacks τ'-dynamics, confirms that PDO-like variability can emerge through anomalous air-sea heat fluxes alone (Pierce et al. 2001; Dommenget and Latif 2008; Clement et al. 2011; Okumura 2013). In the tropical Pacific, a distinct ENSO imprint on the SST anomaly pattern is evident in the FC (Fig. 5c), reminiscent of the ENSO-like pattern in Zhang et al. (1997). This confirms that when ENSO contributes to Aleutian low variability, the coincident ENSO state projects onto the SST anomaly pattern. No tropical SST anomaly signature emerges when Aleutian low variability is independent of ENSO (Fig. 5a-b).

In the subtropical North Pacific, the SST anomaly response to Aleutian low variability depends on whether ENSO is a forcing or not. When non-ENSO variability drives a deeper Aleutian low, a coherent zonal band of warm SST anomalies emerges throughout the subtropical

North Pacific along ~25°N (Fig. 5a-b). A less coherent version of this pattern is shown in the EOF2 of Pacific SST in Fig. 1b in Deser and Blackmon (1995). This subtropical spatial pattern does not accompany the PDO-like pattern in the western part of the Pacific in observational studies (e.g., Newman et al. 2016) or the FC experiment (Fig. 5c), suggesting that ENSO forcing impacts the subtropical response to Aleutian low variability in some way. This was noticed in Larson et al. (2018b; their Fig. 5), and they hypothesized the differing patterns were due to anomalous wind stress driven Ekman transports (which are absent in MD) damping the Q'_{turb} driven SST anomaly in the FC. Here, we will show that the difference in the subtropical SST response is primarily related to ENSO driven air-sea heat fluxes.

Fig. 6 shows the wintertime Q'_{turb} and SST anomaly patterns associated with a deeper Aleutian low. In the MD, anomalous heat fluxes primarily drive SST variability. Clearly the zonal band of $+Q'_{turb}$ anomalies in the subtropical North Pacific drive the SST warming (Fig. 6a). The climatological winds are northeasterly in this region; therefore, the anomalous southwesterlies (Fig. 7a,b, vectors) decrease the wind speed, reducing the turbulent heat flux out of the ocean (according to the bulk formula) and result in an anomalous warming. Unlike what would be expected in an atmosphere model coupled to a slab ocean (SST anomalies and Q'_{turb} generally overlap spatially), the Q'_{turb} and SST anomalies do not perfectly overlap because the mean ocean circulation can still drive anomalous temperature advection. Comparing the MD and MD_{EqPac} (Fig. 6a-b) reveals how non-ENSO τ'-dynamics modify the patterns. There is little difference in the SST and Q'_{turb} south of 20°N (Fig. 6d), suggesting that τ'-dynamics play an insignificant role. Note that if the NPI index is 3-yr low pass filtered prior to the composite analysis, positive SST and Q'_{turb} are weaker in MD_{EqPac}, suggesting that on multi-year timescales, τ'-dynamics damp the warming south of 20°N which may then reduce the air-sea heat flux anomaly. Between 20-40°N, the MD_{EqPac} SST is cooler than in the MD (Fig. 6d), particularly off the east coast of Japan and the central-western North Pacific. The enhanced SST cooling in these regions is associated with increased positive (downward) Q'_{turb} (Fig. 6d), suggesting that τ'-dynamics are the primary driver of the cooling.

ENSO forcing clearly impacts the SST anomaly and Q'_{turb} patterns associated with a deeper Aleutian low (Fig. 6e). Only when ENSO forcing is included does the subtropical SST response diminish, as in the FC (Fig. 6c). The FC shows no coherent zonal band of $+Q'_{turb}$, suggesting that ENSO teleconnected forcings are modifying the Q'_{turb} pattern in the subtropical North Pacific, likely through enhanced evaporative SST cooling related to the overlying anomalous northeasterlies (Fig. 7c, vectors). The difference plot for FC and MD_{EqPac} (Fig. 6e) shows that when Aleutian low variability includes ENSO forcing, significant differences emerge in the Q'_{turb} forcing south of 40°N. For a deeper Aleutian low, ENSO drives $-Q'_{turb}$ in the extratropical interior North Pacific, canceling out the $+Q'_{turb}$ generated on the southern flank of the deepened Aleutian low. South of Japan near the Philippines, ENSO drives $+Q'_{turb}$, likely due to changes in surface winds (Fig. 7c, vectors).

To verify that the Q'_{turb} associated with El Niño and, separately, a deeper Aleutian low differ and oppose each other in the subtropics, we calculate partial regression maps for ERA5, NCEP/NCAR reanalysis, and the FC experiment. The NCEP/NCAR results are not shown, as the results are similar to the ERA5 results. We define the wintertime Niño-3.4 and NPI indexes as the two predictor variables of wintertime Q'_{turb}. The NPI index is multiplied by -1.0 such that the two predictor time series are associated with the same phasing of the Aleutian low (e.g., +Niño-3.4 and –NPI are associated with a deeper Aleutian low). For example, the ENSO partial regression map shows the standardized rate of change of Q'_{turb} per unit change in Nino3.4 with the condition that the NPI is held constant. The goal is to see if the same Q'_{turb} patterns associated with non-ENSO Aleutian low variability (e.g., Fig. 6a-b) and ENSO forcing (Fig. 6e) can emerge from datasets containing the combined forcings. This also provides a sanity check that the spatial patterns in the model are realistic. The ENSO Q'_{turb} pattern in FC (Fig. 8a) closely resembles the ENSO forcing pattern in Fig. 6e, verifying that the pattern is extractable from the FC experiment. The ERA5 pattern matches closely (Fig. 8c), although larger $-Q'_{turb}$ are present in the west Pacific subtropics than the model. A pattern correlation of 0.63 is calculated between the ERA5 and FC ENSO patterns after the ERA5 pattern is coarsened to match the 1° resolution of the model (Fig. 8c-d show the 0.25° resolution). The Q'_{turb} pattern associated with Aleutian low variability is similar between the FC and ERA5 (Fig. 8b,d), confirming that in the absence of ENSO signal interference, a deeper Aleutian low drives a $+Q'_{turb}$ into the subtropical ocean, and this general pattern is extractable and similar in the model and popular reanalysis products. The pattern correlation between the model and ERA5 is 0.76. So, whether there is a subtropical SST response in the western Pacific to Aleutian low variability appears dependent on whether ENSO is a contributing factor or not.

Next, we determine if the anomalous wind stress driven Ekman heat fluxes (Q'_{ek}), an important dynamical forcing of PDO-like SST anomalies (e.g., Alexander and Scott 2008), can explain the differences between the SST anomaly patterns between the experiments (Fig. 6d-e). To assess this contribution, we calculate the Q'_{ek} pattern in Fig. 7, defined as

$$Q'_{ek} = \frac{c_p}{f}\left(\frac{\partial \overline{SST}}{\partial y}\tau'_x - \frac{\partial \overline{SST}}{\partial x}\tau'_y\right), \qquad (1)$$

where c_p is the heat capacity of the ocean, f is the Coriolis parameter, τ_x' and τ_y' are the zonal and meridional wind stress anomalies, respectively, and $\frac{\partial \overline{SST}}{\partial x}$ and $\frac{\partial \overline{SST}}{\partial y}$ are the climatological wintertime zonal and meridional SST gradient, respectively. Ekman due to mean wind stress blowing perpendicular to anomalous SST gradients is not included in the calculation, as Small et al. (2020) show that the wind stress anomaly contribution is more influential on extratropical large-scale SST. The contribution from anomalous SST gradients is indeed generally an order of magnitude smaller than that from anomalous wind stress (not shown). As expected, τ'-dynamics enhance the cool signal in the Kuroshio Extension region (Fig. 6d) through Ekman heat fluxes (Fig. 7a) when the Aleutian low deepens (Alexander 1992; Pierce et al. 2001). Whether ENSO forcing is included or not (Fig. 7a-b) does not impact the Ekman anomaly pattern significantly in most regions (Fig. 7c). One exception is in the western subtropical Pacific, where the wind stress in the FC is more northeasterly and drives an Ekman warming, but these Ekman anomalies are eclipsed by the stronger Q'_{turb} (Fig. 6e). A cooling contribution from Ekman due to anomalous SST gradients counters a small portion of the Ekman warming due to anomalous wind stress (not shown), although the anomalies are too eclipsed by those from Q'_{turb}. ENSO forcing could potentially explain the warmer SST anomaly near 45°N, 160°W and a portion of the colder SST anomaly directly to the south, however neither the differences in Ekman nor the differences in the wind stress anomalies are significantly different.

In the MD_{EqPac}, the wintertime Ekman heat flux anomalies are negative in the North Pacific subtropics where the Q'_{turb} are positive (compare Fig. 6b and Fig. 7a). This is consistent with the Larson et al. (2018b) hypothesis that Ekman plays a damping role to turbulent heat flux forcing in the subtropics, as later demonstrated in Takahashi et al. (2021). However, τ'-dynamics, namely Ekman, appear to play a secondary role to the ENSO-driven Q'_{turb} in damping the subtropical SST response to Aleutian low variability.

As a side note, between 40-45°N off the coast of Japan, the results suggest that a deeper Aleutian low drives a cool SST anomaly through τ'-dynamics (Fig. 6d), whereas ENSO forcing drives a warm SST anomaly (Fig. 6e). Both anomalies coincide with opposite-sign Q'_{turb}, supporting the notion that the ocean forces the atmosphere in this region (Tanimoto et al. 2003). However, it remains unclear why these two forcing mechanisms drive opposite sign SST anomalies. The SST warming associated with ENSO forcing occurs despite a stronger contribution from anomalous Ekman cooling (Fig. 7c). It is possible that the enhanced year-to-year ENSO forcing interferes with the oceanic Rossby wave adjustments to Aleutian low variability, which takes about 4-5 years and acts to enhance SST response in this region (e.g., Miller et al. 1998; Deser et al. 1999; Kwon and Deser 2007; Taguchi et al. 2007).

b. Precipitation over North America

The above analysis establishes that τ'-dynamics and ENSO modify the Q'_{turb} and SST anomaly response to Aleutian low variability. To what extent does inclusion of these processes modify the precipitation patterns over North America? In this section, we also show atmospheric circulation patterns to validate the model results with expectations from the literature. The SLP anomaly composites show that in the absence of ENSO, a deeper Aleutian low is associated with negative SLP anomalies over the southeast U.S. and Mediterranean Sea (Fig. 5a-b). Between these low pressure anomaly centers lies ridging. Consistent with Trenberth et al. (1998), ENSO drives a more enhanced and zonally elongated SLP teleconnection pattern stretching across the Atlantic Ocean (Fig. 5c), whereas when ENSO forcing is absent, the SLP pattern is wavier over the same region (Fig. 5a-b).

The wintertime composite average precipitation anomalies (Fig. 9) show striking differences in the southeast U.S. depending on whether ENSO contributes or does not contribute to Aleutian low variability. In the absence of ENSO, a deeper Aleutian low is associated with reduced precipitation throughout the southern and eastern U.S. and enhanced precipitation in the Pacific Northwest and throughout the Caribbean extending northeastward over the Atlantic Ocean (Fig. 9a-b). When ENSO contributes to Aleutian low variability as in the FC, the ENSO forcing contribution (Fig. 9e) erodes the negative precipitation anomaly in the southeast, allowing the positive precipitation anomalies in the Caribbean to expand northwestward into the southeast (Fig. 9c). Similarly, on the west coast, ENSO forcing results in a positive precipitation anomaly, consistent with a deeper and eastward-extended Aleutian low (Fig. 5c). The ENSO forcing contribution (Fig. 9e) shows a canonical El Niño precipitation pattern, with enhanced precipitation across the southern U.S. (e.g, Ropelewski and Halpert 1987). These results show that ENSO forcing significantly modifies the precipitation signal associated with Aleutian low variability. The impact of τ'-dynamics appears to resemble the ENSO forcing pattern slightly (Fig. 9d). This is likely due to MD_{EqPac} containing more Niño-3.4 variability than MD (Fig. 2). Note that the western US wet anomaly associated with ENSO is not significant in DJF but is in JFM, suggesting that the later months in the NDJFM average contribute most to that feature (e.g., (Deser et al. 2012; Chen et al. 2020; Chapman et al. 2021).

To see if these different spatial patterns are extractable from the FC and observations, partial regression maps are computed for precipitation (Fig. 10). Similar to that done for the Q'_{turb} patterns (e.g., Fig. 8), wintertime Niño-3.4 and the inverted NPI time series are used as the predictors of the wintertime precipitation anomalies. Since precipitation is a noisier variable, we use the NCEP/NCAR reanalysis data from 1948-2020 for the SLP variable instead of ERA5 to match the longer time period of the precipitation dataset. Both the FC experiment and observations show enhanced precipitation in the southern U.S. associated with ENSO (Fig. 10a,c), with maximum anomalies in the southeast. The model generates a stronger pattern in the southeast and west coast, likely related to the too regular and too strong ENSO cycle in the model compared to observations. Overall, both datasets generally resemble the derived ENSO forcing contribution (Fig. 9e). The partial regression technique also extracts a precipitation pattern very similar to that associated with non-ENSO Aleutian low variability (compare Fig. 10b and Fig. 9a-b). This pattern is characterized by reduced precipitation across the south and east U.S. and enhanced precipitation in the Pacific northwest, Caribbean, and subtropical west Atlantic. In observations, the enhanced precipitation signals are substantially weaker than in the model but most importantly, the reduced precipitation signal in the southeast U.S. emerges. This provides further support that in the absence of ENSO, a deeper Aleutian low is associated with negative precipitation anomalies in the southeast U.S.; these anomalies are eroded by El Niño driven positive precipitation anomalies when ENSO forcing is included. The anomaly patterns over the continental U.S. are consistent with the regions of maximum precipitation variance associated with ENSO and the PNA in a prior study (Li et al. 2019). The related 500 hPa partial regression patterns overlay the precipitation patterns in Fig. 10. The patterns for ENSO and the Aleutian low are consistent with the mid-level circulation patterns for tropical Pacific SST and North Pacific SST forcing in prior studies (see Deser and Blackmon 1995; their Fig. 3).

Next, we view the upper atmospheric circulation patterns to hypothesize why these differences in the precipitation pattern may occur. Fig. 11 (contours) shows the wintertime 200 hPa stream function anomalies from the experiments. When Aleutian low variability is driven by non-ENSO sources, a mid-latitude stationary Rossby wave train resembling PNA is evident (Fig. 11a-b), consistent with prior studies (e.g., Deser and Blackmon 1995; Wang et al. 2012; Zhang et al. 2018; Li et al. 2019). Including τ'-dynamics does not substantially impact the PNA pattern (Fig. 11d). When ENSO forcing is present, a more complex pattern emerges, as the anomalies become more interhemispheric and extend into the Southern Hemisphere. The ENSO forcing contribution shows a typical El Niño pattern, consistent with prior studies (Trenberth et al. 1998; Alexander et al. 2002; Straus and Shukla 2002; Li et al. 2019; Chapman et al. 2021).

Composites of the wintertime 200 hPa zonal wind anomalies show a deeper Aleutian low is associated with a stronger and eastward-extended North Pacific jet (Fig. 12a-c). Downstream over North America just west of where the climatological jet splits, a deeper Aleutian low unrelated to ENSO is associated with a southward shift in the jet (Fig. 12a-b). The amplified North Pacific SST response to Aleutian low variability when τ'-dynamics are present modestly enhances the jet response over the Pacific (Fig. 12d). Inclusion of ENSO forcing (Fig. 12c,e), leads to more a pronounced southward shift and zonal elongation of the jet over North America consistent with Seager et al. (2005).

The wintertime 200 hPa velocity divergence anomalies (Fig. 11, shading) also exhibit substantial differences when ENSO forcing is included. When Aleutian low variability is independent of ENSO, anomalous divergence occurs on the east side of the anomalous cyclonic circulation over the North Pacific (Fig. 11a-b), which coincides with the left exit region of the enhanced jet streak (Fig. 12a-b) and enhanced precipitation that stretches over the Pacific Northwest (Fig. 9a-b). Conversely, anomalous convergence occurs on the east side of the anomalous anticyclonic circulation in the subtropical Pacific, which coincides with the right exit region of the enhanced jet streak (Fig. 12a-b) and reduced precipitation stretching into the southwest U.S. (Fig. 9a-b). Upper level anomalous convergence occurs over much of the central, eastern, and southern U. S., directly above the reduced precipitation (Fig. 9a-b). Anomalous upper level divergence also occurs at the east side of the anomalous cyclonic circulation anomaly just off the U.S. east coast, which coincides with the left exit region of the southward shifted 200 hPa jet anomaly (Fig. 12a-b) and enhanced precipitation (Fig. 9a-b). This anomalous divergence pattern is offshore in MD and MD_{EqPac} and extends northwestward when ENSO forcing is present (Fig. 11c). The inclusion of ENSO forcing leads to more conducive upper level dynamics (e.g., a more divergent upper level atmosphere, Fig. 12e) for enhanced precipitation over the southeast United States, which opposes the convergence that occurs when the deeper Aleutian low is independent of ENSO. This shift is due to the zonally elongated flow pattern when El Niño contributes to the deepened Aleutian low, allowing for the upper level cyclonic circulation to extend unimpeded into the southeast and off the mid-Atlantic coast, as seen in the ENSO forcing contribution (Fig. 11e). Although not shown, we would also expect this additional cyclonic circulation to enhance moisture flux convergence in the southeast, as expected with El Niño (e.g., Seager et al. 2005). When the deepened Aleutian low is unrelated to ENSO, there is no ENSO teleconnection to interfere with the stationary Rossby wave response in the extratropics, allowing the ridging over Northern Canada to remain intact, interrupting the cyclonic circulations upstream and downstream.

Finally, we note that only when ENSO contributes to Aleutian low variability and associated SST response do interhemispheric signals emerge in the atmospheric circulation. In the absence of ENSO, Aleutian low variability shows no Southern Hemisphere signal in either SLP (Fig. 5a-b) or the 200 hPa circulation (Fig. 11a-b and Fig. 12a-b). The addition of ENSO forcing drives a Southern Hemisphere SLP signal in the south Indian Ocean (Fig. 5c) as well as shifts in the Southern Hemisphere 200 hPa jet (Fig. 12a-e).

6. Summary and Discussion

This study uses a coupled model experimental approach to determine the extent to which ENSO teleconnections and τ'-dynamics modify the SST response and North American precipitation patterns associated with wintertime Aleutian low variability. We use three CESM1-CAM4 coupled model experiments. The FC experiment is the fully coupled version in which all typical forcings, including ENSO and non-ENSO atmospheric variability, can drive Aleutian low variability, and τ'-dynamics and air-sea heat flux anomalies can drive the SST response (See Table 1). In MD_{EqPac}, ENSO variability is absent and Aleutian low variability is generated primarily via intrinsic atmospheric variability. All non-ENSO τ'-dynamics and air-sea heat fluxes can drive the SST response. In the MD, anomalous wind stress is decoupled from the ocean globally, therefore Aleutian low variability is due only to non-ENSO sources and the SST response is primarily driven by air-sea heat fluxes.

We find that in the absence of ENSO, a deeper wintertime Aleutian low can drive a +PDO-like SST response primarily via air-sea heat flux anomalies (e.g., in MD; Fig. 5a and Fig. 6a), consistent with prior studies (Pierce et al. 2001; Dommenget and Latif 2008; Clement et al. 2011; Okumura 2013). Notably, we find that non-ENSO Aleutian low variability drives a zonal band of SST warming in the subtropical North Pacific that is not present in observations or FC. This subtropical SST signal is driven primarily through Q'_{turb} along the southern flank of the Aleutian low (Fig. 6a). If ENSO forcing also drives the Aleutian low variability, the tropical heating and associated alteration in the near-surface winds drive a Q'_{turb} teleconnection pattern that counteracts that generated by the deeper Aleutian low in the subtropics (Fig. 6). This teleconnection results in a damping of the subtropical SST anomaly response to the Aleutian low variability, resulting in the PDO-like pattern typically seen in observations and the FC, which are devoid of a coherent subtropical SST signal. Therefore, the spatial pattern of the canonical PDO-like response to Aleutian low variability is shaped, in part, by ENSO teleconnections. Although our investigation focuses on wintertime variations, the results suggest that ENSO forcing may be required to reproduce the canonical PDO pattern. We note the possibility that high frequency wind variability unrelated to ENSO could rectify onto longer term variability in subtropics. However, this rectification is likely facilitated through the impact of wind variability on the mean mixed layer depth, which is shown to be minimally impacted in the Pacific subtropics in the MD (Larson et al. 2018b).

ENSO forcing also impacts the atmospheric circulation pattern associated with the Aleutian low. Non-ENSO Aleutian low variability is typically associated with a coherent stationary Rossby wave train resembling the PNA pattern (Fig. 11a,b), consistent with previous studies (e.g., Deser and Blackmon 1995; Wang et al. 2012; Zhang et al. 2018; Li et al. 2019). The pattern is strictly confined over the North Pacific and North America. ENSO forcing acts to interfere with this pattern (Fig. 11c-e), driving an elongation of the cyclonic circulation anomalies in the North Pacific across North America (Trenberth et al. 1998; Alexander et al. 2002; Straus and Shukla 2002; Li et al. 2019; Chapman et al. 2021). Notably, when ENSO is a factor, anomalous upper level divergence promotes enhanced precipitation over the southeast U.S. (Fig. 11e, Fig. 9e), whereas when ENSO is not a factor, anomalous upper level convergence results in reduced precipitation over the southeast (Fig. 11a-b, Fig. 9a-b). We acknowledge that moisture transports are also likely to play a role in these differences (e.g., Seager et al. 2005). Results show that a deeper Aleutian low that includes ENSO forcing drives the enhanced precipitation signal in the southeast typically associated with the PDO (e.g., Newman et al. 2016). Without ENSO forcing, the patterns are significantly modified, yielding enhanced dryness across the eastern and central U.S., including in the southeast.

We acknowledge that some details of the analyses could be model dependent; however, the two most important conclusions are supported by observational evidence, as shown in the partial regression maps (Fig. 8 and Fig. 10). First, the destructive interference of the ENSO-driven Q'_{turb} teleconnection with the Q'_{turb} generated by Aleutian variability in the subtropical North Pacific is reproduced in two popular reanalysis products. Second, the negative precipitation signal in the southeast U.S. generated via a deeper Aleutian low without ENSO forcing is also reproduced in two reanalysis products and is extractable from the FC.

Given that a PDO-like SST pattern is typically associated with Aleutian low variability, we conclude by discussing studies attempting to understand how ENSO modifies climate anomalies associated with the PDO. Using conditional composite analysis of ENSO and the PDO, Hu and Huang (2009) argue that without ENSO variability, the PDO has no significant climate impact over North America. We find that when ENSO forcing is not included in the Aleutian low variability and the associated PDO-like SST response, there is a significant difference in the precipitation pattern over the southeast and west coast of the United States compared to when ENSO is included. This discrepancy is likely related to the small sample size in their study.

Wang et al. (2012) analyze the PDO in the NCEP CFS model with tropical Pacific SST either relaxed to climatology or time varying, which includes ENSO variability. Zhang et al. (2018) use a similar approach with a different model. In the Wang et al. (2012) study, there is a hint of a subtropical warming signal associated with the PDO in their “No-ENSO” run. The authors suggest it may be related to slightly different atmospheric circulation patterns over the region. We find that the subtropical warming pattern is directly related to ENSO’s teleconnected Q'_{turb}, which appear to be related to weak anomalous northeasterlies forced by ENSO (Fig. 7c).

Wang et al. (2012) also argue that the precipitation patterns associated with the PDO and ENSO are approximately linear, although their linear approximation misses the opposite-sign precipitation response in the southeast U.S. (their Fig. 10d) during +PDO/–NPI. Our results, while focused solely on relationships with wintertime Aleutian low variability, suggest that precipitation patterns associated with ENSO and non-ENSO Aleutian low variability are approximately linear, as our partial regression analysis confirms that the non-ENSO related precipitation pattern (Fig. 9a-b) can be separated from the ENSO pattern in both observations and the FC (Fig. 10). Furthermore, our results show strong evidence of a robust dry precipitation anomaly occurring throughout the southern and eastern U.S. during –NPI winters, which is associated with a +PDO-like SST pattern, which has not been highlighted in prior studies. This could be due to small sample sizes of observational studies or caveats related to prescribed SST experiments, as mentioned earlier.

There are many implications based on these results. First, it is clear that model simulation of ENSO teleconnection patterns is crucial to obtaining realistic climate anomalies associated with Aleutian low variability. For example, Yim et al. (2015) show the PDO pattern for multiple CMIP5 models (albeit the domain only extends to 20°N), and many models simulate a subtropical SST signal that is not seen in nature. We hypothesize this discrepancy may be related to errors in the ENSO driven air-sea heat fluxes, as many coupled models, even in CMIP6, have issues in simulating a realistic ENSO teleconnection pattern (Planton et al. 2021). Models with realistic ENSO teleconnections should be preferentially used for PDO, Aleutian low, and wintertime North American climate prediction applications and studies.

Second, our results suggest that during winters when non-ENSO variability results in a persistent, deeper Aleutian low, the resulting SST response in the North Pacific and the precipitation teleconnection downstream to the southeast U.S. will be different had El Niño contributed to the Aleutian low deepening. The different precipitation responses in the southeast U.S. to different sources of Aleutian low variability may have implications for seasonal climate prediction over North America. Additional analyses need to be conducted to determine if the precipitation pattern associated with non-ENSO Aleutian low variability are predictable on seasonal timescales, but that is outside the scope of this work. For example, ENSO is thought to be the primary source of predictability for atmospheric variability over North America (Jha et al. 2019; Li et al. 2019). Based on our results, one would expect that during winters when El Niño contributes to driving a deeper Aleutian low and a positive PDO-like response, the expected precipitation response over North America follows the canonical PDO, with enhanced precipitation in the southeast. However, when a persistent deeper Aleutian low develops independent of ENSO, negative precipitation anomalies occur over the southeast.

Acknowledgements

This work was supported by NSF grant AGS-1951713 (SML). ERA5 datasets were obtained freely from Copernicus Climate Change service at https://doi.org/10.24381/cds.f17050d7. PREC Precipitation is provided by the NOAA/OAR/ESRL PSL, Boulder, Colorado, USA, from their website at https://psl.noaa.gov/data/gridded/data.prec.html. NCEP/NCAR Reanalysis is provided by the NOAA/OAR/ESRL PSL, Boulder, Colorado, USA, from their website at https://psl.noaa.gov/data/gridded/data.ncep.reanalysis.html. Source code for the CESM1-CAM4 experiments is freely available from NCAR. We also acknowledge the high-performance computing support from Cheyenne (https://doi.org/10.5065/D6RX99HX) provided by NCAR's Computational and Information Systems Laboratory, sponsored by NSF. We thank three anonymous reviewers for their helpful comments and suggestions.

References

Adler, R. F., and Coauthors, 2003: The Version-2 Global Precipitation Climatology Project (GPCP) Monthly Precipitation Analysis (1979–Present). *Journal of Hydrometeorology*, **4**, 1147–1167, https://doi.org/10.1175/1525-7541(2003)004<1147:TVGPCP>2.0.CO;2.

Alexander, M., 2010: Extratropical air-sea interaction, sea surface temperature variability, and the Pacific Decadal Oscillation. *Geophysical Monograph Series*, D.-Z. Sun and F. Bryan, Eds., Vol. 189 of, American Geophysical Union, 123–148.

Alexander, M. A., 1992: Midlatitude Atmosphere–Ocean Interaction during El Niño. Part I: The North Pacific Ocean. *Journal of Climate*, **5**, 944–958, https://doi.org/10.1175/1520-0442(1992)005<0944:MAIDEN>2.0.CO;2.

——, and C. Deser, 1995: A Mechanism for the Recurrence of Wintertime Midlatitude SST Anomalies. *J. Phys. Oceanogr.*, **25**, 122–137, https://doi.org/10.1175/1520-0485(1995)025<0122:AMFTRO>2.0.CO;2.

——, and J. D. Scott, 2008: The Role of Ekman Ocean Heat Transport in the Northern Hemisphere Response to ENSO. *Journal of Climate*, **21**, 5688–5707, https://doi.org/10.1175/2008JCLI2382.1.

——, C. Deser, and M. S. Timlin, 1999: The Reemergence of SST Anomalies in the North Pacific Ocean. *J. Climate*, **12**, 2419–2433, https://doi.org/10.1175/1520-0442(1999)012<2419:TROSAI>2.0.CO;2.

——, I. Bladé, M. Newman, J. R. Lanzante, N.-C. Lau, and J. D. Scott, 2002: The Atmospheric Bridge: The Influence of ENSO Teleconnections on Air–Sea Interaction over the Global Oceans. *Journal of Climate*, **15**, 2205–2231, https://doi.org/10.1175/1520-0442(2002)015<2205:TABTIO>2.0.CO;2.

Anderson, B. T., and R. C. Perez, 2015: ENSO and non-ENSO induced charging and discharging of the equatorial Pacific. *Climate Dynamics*, **45**, 2309–2327, https://doi.org/10.1007/s00382-015-2472-x.

Blackmon, M. L., J. E. Geisler, and E. J. Pitcher, 1983: A General Circulation Model Study of January Climate Anomaly Patterns Associated with Interannual Variation of Equatorial Pacific Sea Surface Temperatures. *Journal of the Atmospheric Sciences*, **40**, 1410–1425, https://doi.org/10.1175/1520-0469(1983)040<1410:AGCMSO>2.0.CO;2.

Brown, D. P., and A. C. Comrie, 2004: A winter precipitation 'dipole' in the western United States associated with multidecadal ENSO variability. *Geophysical Research Letters*, **31**, https://doi.org/10.1029/2003GL018726.

Cayan, D. R., M. D. Dettinger, H. F. Diaz, and N. E. Graham, 1998: Decadal Variability of Precipitation over Western North America. *Journal of Climate*, **11**, 3148–3166, https://doi.org/10.1175/1520-0442(1998)011<3148:DVOPOW>2.0.CO;2.

Chakravorty, S., R. C. Perez, B. T. Anderson, B. S. Giese, S. M. Larson, and V. Pivotti, 2020: Testing the Trade Wind Charging Mechanism and Its Influence on ENSO Variability. *Journal of Climate*, **33**, 7391–7411, https://doi.org/10.1175/JCLI-D-19-0727.1.

Chapman, W. E., A. C. Subramanian, S.-P. Xie, M. D. Sierks, F. M. Ralph, and Y. Kamae, 2021: Monthly Modulations of ENSO Teleconnections: Implications for Potential Predictability in North America. *Journal of Climate*, **34**, 5899–5921, https://doi.org/10.1175/JCLI-D-20-0391.1.

Chen, M., P. Xie, J. E. Janowiak, and P. A. Arkin, 2002: Global Land Precipitation: A 50-yr Monthly Analysis Based on Gauge Observations. *Journal of Hydrometeorology*, **3**, 249–266, https://doi.org/10.1175/1525-7541(2002)003<0249:GLPAYM>2.0.CO;2.

Chen, R., I. R. Simpson, C. Deser, and B. Wang, 2020: Model Biases in the Simulation of the Springtime North Pacific ENSO Teleconnection. *Journal of Climate*, **33**, 9985–10002, https://doi.org/10.1175/JCLI-D-19-1004.1.

Clement, A., P. DiNezio, and C. Deser, 2011: Rethinking the Ocean's Role in the Southern Oscillation. *Journal of Climate*, **24**, 4056–4072, https://doi.org/10.1175/2011JCLI3973.1.

Cole, J. E., J. T. Overpeck, and E. R. Cook, 2002: Multiyear La Niña events and persistent drought in the contiguous United States. *Geophysical Research Letters*, **29**, 25-1-25–4, https://doi.org/10.1029/2001GL013561.

Dai, A., K. E. Trenberth, and T. R. Karl, 1998: Global variations in droughts and wet spells: 1900–1995. *Geophysical Research Letters*, **25**, 3367–3370, https://doi.org/10.1029/98GL52511.

Deser, C., and M. L. Blackmon, 1995: On the Relationship between Tropical and North Pacific Sea Surface Temperature Variations. *Journal of Climate*, **8**, 1677–1680, https://doi.org/10.1175/1520-0442(1995)008<1677:OTRBTA>2.0.CO;2.

——, and A. S. Phillips, 2006: Simulation of the 1976/77 Climate Transition over the North Pacific: Sensitivity to Tropical Forcing. *Journal of Climate*, **19**, 6170–6180, https://doi.org/10.1175/JCLI3963.1.

——, M. A. Alexander, and M. S. Timlin, 1999: Evidence for a Wind-Driven Intensification of the Kuroshio Current Extension from the 1970s to the 1980s. *Journal of Climate*, **12**, 1697–1706, https://doi.org/10.1175/1520-0442(1999)012<1697:EFAWDI>2.0.CO;2.

——, and Coauthors, 2012: ENSO and Pacific Decadal Variability in the Community Climate System Model Version 4. *Journal of Climate*, **25**, 2622–2651, https://doi.org/10.1175/JCLI-D-11-00301.1.

Di Lorenzo, E., and M. D. Ohman, 2013: A double-integration hypothesis to explain ocean ecosystem response to climate forcing. *Proceedings of the National Academy of Sciences*, **110**, 2496–2499, https://doi.org/10.1073/pnas.1218022110.

Di Lorenzo, E., and N. Mantua, 2016: Multi-year persistence of the 2014/15 North Pacific marine heatwave. *Nature Clim Change*, **6**, 1042–1047, https://doi.org/10.1038/nclimate3082.

Dommenget, D., 2010: The slab ocean El Niño. *Geophysical Research Letters*, **37**, https://doi.org/10.1029/2010GL044888.

Dommenget, D., and M. Latif, 2008: Generation of hyper climate modes. *Geophysical Research Letters*, **35**, https://doi.org/10.1029/2007GL031087.

Gent, P. R., and Coauthors, 2011: The Community Climate System Model Version 4. *Journal of Climate*, **24**, 4973–4991, https://doi.org/10.1175/2011JCLI4083.1.

Gershunov, A., and T. P. Barnett, 1998: Interdecadal Modulation of ENSO Teleconnections. *Bulletin of the American Meteorological Society*, **79**, 2715–2726, https://doi.org/10.1175/1520-0477(1998)079<2715:IMOET>2.0.CO;2.

Hersbach, H., B. Bell, P. Berrisford, and coauthors, 2020: The ERA5 global reanalysis - Hersbach - 2020 - Quarterly Journal of the Royal Meteorological Society - Wiley Online Library. https://rmets.onlinelibrary.wiley.com/doi/full/10.1002/qj.3803 (Accessed July 19, 2021).

Hoerling, M. P., and A. Kumar, 2002: Atmospheric Response Patterns Associated with Tropical Forcing. *Journal of Climate*, **15**, 2184–2203, https://doi.org/10.1175/1520-0442(2002)015<2184:ARPAWT>2.0.CO;2.

Hu, Z.-Z., and B. Huang, 2009: Interferential Impact of ENSO and PDO on Dry and Wet Conditions in the U.S. Great Plains. *Journal of Climate*, **22**, 6047–6065, https://doi.org/10.1175/2009JCLI2798.1.

Hurrell, J. W., and Coauthors, 2013: The Community Earth System Model: A Framework for Collaborative Research. *Bulletin of the American Meteorological Society*, **94**, 1339–1360, https://doi.org/10.1175/BAMS-D-12-00121.1.

Jha, B., and A. Kumar, 2009: A Comparison of the Atmospheric Response to ENSO in Coupled and Uncoupled Model Simulations. *Monthly Weather Review*, **137**, 479–487, https://doi.org/10.1175/2008MWR2489.1.

——, ——, and Z.-Z. Hu, 2019: An update on the estimate of predictability of seasonal mean atmospheric variability using North American Multi-Model Ensemble. *Clim Dyn*, **53**, 7397–7409, https://doi.org/10.1007/s00382-016-3217-1.

Johnson, N. C., and S. B. Feldstein, 2010: The Continuum of North Pacific Sea Level Pressure Patterns: Intraseasonal, Interannual, and Interdecadal Variability. *Journal of Climate*, **23**, 851–867, https://doi.org/10.1175/2009JCLI3099.1.

Kalnay, E., and Coauthors, 1996: The NCEP/NCAR 40-Year Reanalysis Project. *Bulletin of the American Meteorological Society*, **77**, 437–472, https://doi.org/10.1175/1520-0477(1996)077<0437:TNYRP>2.0.CO;2.

Kiem, A. S., S. W. Franks, and G. Kuczera, 2003: Multi-decadal variability of flood risk. *Geophysical Research Letters*, **30**, https://doi.org/10.1029/2002GL015992.

Kumar, A., and H. Wang, 2015: On the potential of extratropical SST anomalies for improving climate predictions. *Clim Dyn*, **44**, 2557–2569, https://doi.org/10.1007/s00382-014-2398-8.

——, ——, W. Wang, Y. Xue, and Z.-Z. Hu, 2013: Does Knowing the Oceanic PDO Phase Help Predict the Atmospheric Anomalies in Subsequent Months? *Journal of Climate*, **26**, 1268–1285, https://doi.org/10.1175/JCLI-D-12-00057.1.

Kwon, Y.-O., and C. Deser, 2007: North Pacific Decadal Variability in the Community Climate System Model Version 2. *Journal of Climate*, **20**, 2416–2433, https://doi.org/10.1175/JCLI4103.1.

Larson, S. M., and B. P. Kirtman, 2015: Revisiting ENSO Coupled Instability Theory and SST Error Growth in a Fully Coupled Model. *Journal of Climate*, **28**, 4724–4742, https://doi.org/10.1175/JCLI-D-14-00731.1.

——, ——, and D. J. Vimont, 2017: A Framework to Decompose Wind-Driven Biases in Climate Models Applied to CCSM/CESM in the Eastern Pacific. *Journal of Climate*, **30**, 8763–8782, https://doi.org/10.1175/JCLI-D-17-0099.1.

——, K. V. Pegion, and B. P. Kirtman, 2018a: The South Pacific Meridional Mode as a Thermally Driven Source of ENSO Amplitude Modulation and Uncertainty. *Journal of Climate*, **31**, 5127–5145, https://doi.org/10.1175/JCLI-D-17-0722.1.

——, D. J. Vimont, A. C. Clement, and B. P. Kirtman, 2018b: How Momentum Coupling Affects SST Variance and Large-Scale Pacific Climate Variability in CESM. *Journal of Climate*, **31**, 2927–2944, https://doi.org/10.1175/JCLI-D-17-0645.1.

——, M. W. Buckley, and A. C. Clement, 2020: Extracting the Buoyancy-Driven Atlantic Meridional Overturning Circulation. *Journal of Climate*, **33**, 4697–4714, https://doi.org/10.1175/JCLI-D-19-0590.1.

Latif, M., and T. P. Barnett, 1996: Decadal Climate Variability over the North Pacific and North America: Dynamics and Predictability. *Journal of Climate*, **9**, 2407–2423, https://doi.org/10.1175/1520-0442(1996)009<2407:DCVOTN>2.0.CO;2.

Lau, N.-C., 1997: Interactions between Global SST Anomalies and the Midlatitude Atmospheric Circulation. *Bulletin of the American Meteorological Society*, **78**, 21–34, https://doi.org/10.1175/1520-0477(1997)078<0021:IBGSAA>2.0.CO;2.

——, and M. J. Nath, 1994: A Modeling Study of the Relative Roles of Tropical and Extratropical SST Anomalies in the Variability of the Global Atmosphere-Ocean System. *Journal of Climate*, **7**, 1184–1207, https://doi.org/10.1175/1520-0442(1994)007<1184:AMSOTR>2.0.CO;2.

Li, X., Z.-Z. Hu, P. Liang, and J. Zhu, 2019: Contrastive Influence of ENSO and PNA on Variability and Predictability of North American Winter Precipitation. *Journal of Climate*, **32**, 6271–6284, https://doi.org/10.1175/JCLI-D-19-0033.1.

Liu, Z., and M. Alexander, 2007: Atmospheric bridge, oceanic tunnel, and global climatic teleconnections. *Reviews of Geophysics*, **45**, https://doi.org/10.1029/2005RG000172.

Livezey, R. E., and K. C. Mo, 1987: Tropical-Extratropical Teleconnections during the Northern Hemisphere Winter. Part II: Relationships between Monthly Mean Northern Hemisphere Circulation Patterns and Proxies for Tropical Convection. *Monthly Weather Review*, **115**, 3115–3132, https://doi.org/10.1175/1520-0493(1987)115<3115:TETDTN>2.0.CO;2.

Mantua, N. J., S. R. Hare, Y. Zhang, J. M. Wallace, and R. C. Francis, 1997: A Pacific Interdecadal Climate Oscillation with Impacts on Salmon Production*. *Bulletin of the American Meteorological Society*, **78**, 1069–1080, https://doi.org/10.1175/1520-0477(1997)078<1069:APICOW>2.0.CO;2.

McAfee, S. A., 2014: Consistency and the Lack Thereof in Pacific Decadal Oscillation Impacts on North American Winter Climate. *Journal of Climate*, **27**, 7410–7431, https://doi.org/10.1175/JCLI-D-14-00143.1.

McCabe, G. J., and M. D. Dettinger, 1999: Decadal variations in the strength of ENSO teleconnections with precipitation in the western United States. *International Journal of Climatology*, **19**, 1399–1410, https://doi.org/10.1002/(SICI)1097-0088(19991115)19:13<1399::AID-JOC457>3.0.CO;2-A.

Miller, A. J., and N. Schneider, 2000: Interdecadal climate regime dynamics in the North Pacific Ocean: theories, observations and ecosystem impacts. *Progress in Oceanography*, **47**, 355–379, https://doi.org/10.1016/S0079-6611(00)00044-6.

Miller, A. J., D. R. Cayan, T. P. Barnett, N. E. Graham, and J. M. Oberhuber, 1994: Interdecadal variability of the Pacific Ocean: model response to observed heat flux and wind stress anomalies. *Climate Dynamics*, **9**, 287–302, https://doi.org/10.1007/BF00204744.

——, ——, and W. B. White, 1998: A Westward-Intensified Decadal Change in the North Pacific Thermocline and Gyre-Scale Circulation. *Journal of Climate*, **11**, 3112–3127, https://doi.org/10.1175/1520-0442(1998)011<3112:AWIDCI>2.0.CO;2.

Namias, J., X. Yuan, and D. R. Cayan, 1988: Persistence of North Pacific Sea Surface Temperature and Atmospheric Flow Patterns. *Journal of Climate*, **1**, 682–703, https://doi.org/10.1175/1520-0442(1988)001<0682:PONPSS>2.0.CO;2.

Neale, R. B., J. Richter, S. Park, P. H. Lauritzen, S. J. Vavrus, P. J. Rasch, and M. Zhang, 2013: The Mean Climate of the Community Atmosphere Model (CAM4) in Forced SST and Fully Coupled Experiments. *Journal of Climate*, **26**, 5150–5168, https://doi.org/10.1175/JCLI-D-12-00236.1.

Newman, M., G. P. Compo, and M. A. Alexander, 2003: ENSO-Forced Variability of the Pacific Decadal Oscillation. *Journal of Climate*, **16**, 3853–3857, https://doi.org/10.1175/1520-0442(2003)016<3853:EVOTPD>2.0.CO;2.

——, and Coauthors, 2016: The Pacific Decadal Oscillation, Revisited. *Journal of Climate*, **29**, 4399–4427, https://doi.org/10.1175/JCLI-D-15-0508.1.

Okumura, Y. M., 2013: Origins of Tropical Pacific Decadal Variability: Role of Stochastic Atmospheric Forcing from the South Pacific. *Journal of Climate*, **26**, 9791–9796, https://doi.org/10.1175/JCLI-D-13-00448.1.

——, C. Deser, A. Hu, A. Timmermann, and S.-P. Xie, 2009: North Pacific Climate Response to Freshwater Forcing in the Subarctic North Atlantic: Oceanic and Atmospheric Pathways. *Journal of Climate*, **22**, 1424–1445, https://doi.org/10.1175/2008JCLI2511.1.

——, T. Sun, and X. Wu, 2017: Asymmetric Modulation of El Niño and La Niña and the Linkage to Tropical Pacific Decadal Variability. *Journal of Climate*, **30**, 4705–4733, https://doi.org/10.1175/JCLI-D-16-0680.1.

Pierce, D. W., T. P. Barnett, N. Schneider, R. Saravanan, D. Dommenget, and M. Latif, 2001: The role of ocean dynamics in producing decadal climate variability in the North Pacific. *Climate Dynamics*, **18**, 51–70.

Planton, Y. Y., and Coauthors, 2021: Evaluating Climate Models with the CLIVAR 2020 ENSO Metrics Package. *Bulletin of the American Meteorological Society*, **102**, E193–E217, https://doi.org/10.1175/BAMS-D-19-0337.1.

Power, S., M. Lengaigne, A. Capotondi, and coauthors, 2021: Decadal climate variability in the tropical Pacific: Characteristics, causes, predictability and prospects. *Science*, in review.

Qiu, B., 2003: Kuroshio Extension Variability and Forcing of the Pacific Decadal Oscillations: Responses and Potential Feedback. *Journal of Physical Oceanography*, **33**, 2465–2482, https://doi.org/10.1175/2459.1.

Rayner, N. A., D. E. Parker, E. B. Horton, C. K. Folland, L. V. Alexander, D. P. Rowell, E. C. Kent, and A. Kaplan, 2003: Global analyses of sea surface temperature, sea ice, and night marine air temperature since the late nineteenth century. *Journal of Geophysical Research: Atmospheres,* **108**, https://doi.org/10.1029/2002JD002670.

Ropelewski, C. F., and M. S. Halpert, 1987: Global and Regional Scale Precipitation Patterns Associated with the El Niño/Southern Oscillation. *Monthly Weather Review*, **115**, 1606–1626, https://doi.org/10.1175/1520-0493(1987)115<1606:GARSPP>2.0.CO;2.

——, and ——, 1989: Precipitation Patterns Associated with the High Index Phase of the Southern Oscillation. *Journal of Climate*, **2**, 268–284, https://doi.org/10.1175/1520-0442(1989)002<0268:PPAWTH>2.0.CO;2.

Saravanan, R., and P. Chang, 1999: Oceanic mixed layer feedback and tropical Atlantic variability. *Geophysical Research Letters*, **26**, 3629–3632, https://doi.org/10.1029/1999GL010468.

Schneider, N., and A. J. Miller, 2001: Predicting Western North Pacific Ocean Climate. *Journal of Climate*, **14**, 3997–4002, https://doi.org/10.1175/1520-0442(2001)014<3997:PWNPOC>2.0.CO;2.

——, and B. D. Cornuelle, 2005: The Forcing of the Pacific Decadal Oscillation. *Journal of Climate*, **18**, 4355–4373, https://doi.org/10.1175/JCLI3527.1.

——, A. J. Miller, and D. W. Pierce, 2002: Anatomy of North Pacific Decadal Variability. *Journal of Climate*, **15**, 586–605, https://doi.org/10.1175/1520-0442(2002)015<0586:AONPDV>2.0.CO;2.

Seager, R., Y. Kushnir, N. H. Naik, M. A. Cane, and J. Miller, 2001: Wind-Driven Shifts in the Latitude of the Kuroshio–Oyashio Extension and Generation of SST Anomalies on Decadal Timescales. *Journal of Climate*, **14**, 4249–4265, https://doi.org/10.1175/1520-0442(2001)014<4249:WDSITL>2.0.CO;2.

Seager, R., N. Harnik, W. A. Robinson, Y. Kushnir, M. Ting, H.-P. Huang, and J. Velez, 2005: Mechanisms of ENSO-forcing of hemispherically symmetric precipitation variability. *Quarterly Journal of the Royal Meteorological Society*, **131**, 1501–1527, https://doi.org/10.1256/qj.04.96.

Small, R. J., F. O. Bryan, S. P. Bishop, S. Larson, and R. A. Tomas, 2020: What Drives Upper-Ocean Temperature Variability in Coupled Climate Models and Observations? *Journal of Climate*, **33**, 577–596, https://doi.org/10.1175/JCLI-D-19-0295.1.

Smith, R., and Coauthors, 2010: The Parallel Ocean Program (POP) Reference Manual. 141.

Straus, D. M., and J. Shukla, 2002: Does ENSO Force the PNA? *Journal of Climate*, **15**, 2340–2358, https://doi.org/10.1175/1520-0442(2002)015<2340:DEFTP>2.0.CO;2.

Sun, T., and Y. M. Okumura, 2020: Impact of ENSO-Like Tropical Pacific Decadal Variability on the Relative Frequency of El Niño and La Niña Events. *Geophysical Research Letters*, **47**, e2019GL085832, https://doi.org/10.1029/2019GL085832.

Sutton, R., and P.-P. Mathieu, 2002: Response of the atmosphere–ocean mixed-layer system to anomalous ocean heat-flux convergence. *Quarterly Journal of the Royal Meteorological Society*, **128**, 1259–1275, https://doi.org/10.1256/003590002320373283.

Taguchi, B., S.-P. Xie, N. Schneider, M. Nonaka, H. Sasaki, and Y. Sasai, 2007: Decadal Variability of the Kuroshio Extension: Observations and an Eddy-Resolving Model Hindcast. *Journal of Climate*, **20**, 2357–2377, https://doi.org/10.1175/JCLI4142.1.

Takahashi, N., K. J. Richards, N. Schneider, H. Annamalai, W.-C. Hsu, and M. Nonaka, 2021: Formation Mechanism of Warm SST Anomalies in 2010s Around Hawaii. *Journal of Geophysical Research: Oceans*, **126**, e2021JC017763, https://doi.org/10.1029/2021JC017763.

Tanimoto, Y., H. Nakamura, T. Kagimoto, and S. Yamane, 2003: An active role of extratropical sea surface temperature anomalies in determining anomalous turbulent heat flux. *Journal of Geophysical Research: Oceans*, **108**, https://doi.org/10.1029/2002JC001750.

Trenberth, K. E., 1990: Recent Observed Interdecadal Climate Changes in the Northern Hemisphere. *Bulletin of the American Meteorological Society*, **71**, 988–993, https://doi.org/10.1175/1520-0477(1990)071<0988:ROICCI>2.0.CO;2.

——, and J. W. Hurrell, 1994: Decadal atmosphere-ocean variations in the Pacific. *Climate Dynamics*, **9**, 303–319, https://doi.org/10.1007/BF00204745.

——, G. W. Branstator, D. Karoly, A. Kumar, N.-C. Lau, and C. Ropelewski, 1998: Progress during TOGA in understanding and modeling global teleconnections associated with tropical sea surface temperatures. *Journal of Geophysical Research: Oceans*, **103**, 14291–14324, https://doi.org/10.1029/97JC01444.

Verdon, D. C., and S. W. Franks, 2006: Long-term behaviour of ENSO: Interactions with the PDO over the past 400 years inferred from paleoclimate records. *Geophysical Research Letters*, **33**, https://doi.org/10.1029/2005GL025052.

Vimont, D. J., 2005: The Contribution of the Interannual ENSO Cycle to the Spatial Pattern of Decadal ENSO-Like Variability. *Journal of Climate*, **18**, 2080–2092, https://doi.org/10.1175/JCLI3365.1.

Wallace, J. M., and D. S. Gutzler, 1981: Teleconnections in the Geopotential Height Field during the Northern Hemisphere Winter. *Monthly Weather Review*, **109**, 784–812, https://doi.org/10.1175/1520-0493(1981)109<0784:TITGHF>2.0.CO;2.

Wang, H., A. Kumar, W. Wang, and Y. Xue, 2012: Influence of ENSO on Pacific Decadal Variability: An Analysis Based on the NCEP Climate Forecast System. *Journal of Climate*, **25**, 6136–6151, https://doi.org/10.1175/JCLI-D-11-00573.1.

Yim, B. Y., M. Kwon, H. S. Min, and J.-S. Kug, 2015: Pacific Decadal Oscillation and its relation to the extratropical atmospheric variation in CMIP5. *Clim Dyn*, **44**, 1521–1540, https://doi.org/10.1007/s00382-014-2349-4.

Yulaeva, E., N. Schneider, D. W. Pierce, and T. P. Barnett, 2001: Modeling of North Pacific Climate Variability Forced by Oceanic Heat Flux Anomalies. *Journal of Climate*, **14**, 4027–4046, https://doi.org/10.1175/1520-0442(2001)014<4027:MONPCV>2.0.CO;2.

Zhang, H., A. Clement, and P. Di Nezio, 2014: The South Pacific Meridional Mode: A Mechanism for ENSO-like Variability. *J. Climate*, **27**, 769–783, https://doi.org/10.1175/JCLI-D-13-00082.1.

Zhang, Y., J. M. Wallace, and D. S. Battisti, 1997: ENSO-like Interdecadal Variability: 1900–93. *Journal of Climate*, **10**, 1004–1020, https://doi.org/10.1175/1520-0442(1997)010<1004:ELIV>2.0.CO;2.

Zhang, Y., S.-P. Xie, Y. Kosaka, and J.-C. Yang, 2018: Pacific Decadal Oscillation: Tropical Pacific Forcing versus Internal Variability. *Journal of Climate*, **31**, 8265–8279, https://doi.org/10.1175/JCLI-D-18-0164.1.

Table Captions

Table 1. Summary of each CESM1-CAM4 experiment setup, the sources of Aleutian Low variability in each experiment, and the processes that can drive the SST response to Aleutian Low variability. All experiments include dynamic atmosphere and ocean models, as well as land and sea ice models. All experiments include unconstrained buoyancy (heat and freshwater) fluxes.

Table 2. Event count for anomalously strong (–NPI) and weak (+NPI) wintertime Aleutian low years. For the MD experiment, the event count in parenthesized italics is from a different 300-yr window not used in this analysis to show the low sensitivity of the sample size to the 300-yr window chosen for this experiment. Both MD_{EqPac} and FC are only 300 years total, so a similar sensitivity test is not performed.

Figure Captions

Fig. 1. Annual mean SST climatology (white contours) and monthly SST anomaly variance (shading) for experiments a) MD, b) MD_{EqPac}, c) FC, and d) observations from HadISST. Observations are taken from years 1980-2020 to roughly represent the year 2000 time period (model experiments are run with year 2000 forcing). The SST climatology contours are in 3°C intervals and the 27°C isotherm is in bold. SST variance is in units $(°C)^2$.

Fig. 2. ENSO variability in each experiment as estimated by the monthly Niño-3.4 SST anomaly index, defined as the area-averaged SST anomaly over 5°S-5°N, 170°W-120°W. a) Niño-3.4 SST anomaly index for 120 consecutive years from experiments for the MD, MD_{EqPac}, and FC Experiments. b) Niño-3.4 spectrum for each experiment, computed over the full 300 years of model data.

Fig. 3. a) Variance preserving power spectra of boreal wintertime Aleutian Low variability for the MD, MD_{EqPac}, and FC experiments and reanalysis products. Boreal winter Aleutian low variability is estimated using the NDJFM-averaged North Pacific Index (NPI), defined as the area-averaged sea level pressure anomalies over 30°N-65°N, 160°E-140°W. A 5-point Daniell smoothing is applied to the spectral estimates. For each of the model experiments, the NPI is divided into 60-yr non-overlapping windows, the spectrum is computed for each window, and the average spectra over the windows is displayed. b) Same as a) except each NPI time series is standardized by its own standard deviation prior to spectral analysis.

Fig. 4. Monthly precipitation anomaly variance for a) MD, b) MD_{EqPac}, c) FC, CESM1-CAM4 experiments and d) observations from GPCP 1979-2020. Units are $(\mathrm{mm\ day}^{-1})^2$.

Fig. 5. Composite averaged wintertime SST (shading) and sea level pressure (SLP; black contours) anomalies associated with Aleutian Low variability for the MD, MD_{EqPac}, and FC

experiments. Events are defined as meeting or exceeding +/– one standard deviation of the wintertime NPI. Composites are displayed as [–NPI - (+NPI)] / 2 to reflect the spatial pattern and typical amplitude of a deepened Aleutian Low and the +PDO-like SST anomaly response. SLP contour intervals begin at +/– 0.5 hPa and increase in amplitude in 0.5 hPa intervals. Dashed contours indicate negative SLP anomalies. SST anomalies are in °C. Wintertime months are defined as NDJFM.

Fig. 6. North Pacific composite average wintertime turbulent heat flux (shading) and SST (contours) anomalies associated with Aleutian Low variability for a-c) each model experiment and d-e) their differences. Events are defined as meeting or exceeding +/– one standard deviation of the wintertime NPI. Composites are displayed as [–NPI - (+NPI)] / 2 to reflect the spatial pattern and typical amplitude of anomalies associated with a deepened Aleutian Low. Turbulent heat fluxes are calculated as the sum of the sensible and latent heat flux anomalies. The sign convention is a positive (negative) heat flux is into the ocean, or a warming (cooling) and units are Wm^{-2}. SST anomaly contour intervals begin at +/– 0.1 °C and increase in amplitude in 0.1°C intervals. Negative contours indicate negative SST anomalies. Wintertime months are defined as NDJFM. Stippling in panels d-e indicates turbulent heat flux anomaly differences significant at the 95% confidence level using a two-sided Welch's t-test.

Fig. 7. Similar to Fig. 6b,c,e, except for wintertime anomalous wind stress driven Ekman heat flux (shading) and SST (contours) anomalies. Ekman heat flux anomaly units are Wm^{-2}. SST anomaly contour intervals begin at +/– 0.1 °C and increase in amplitude in 0.1°C intervals. Magenta vectors are the composite wind stress anomaly in units Nm^{-2}. Stippling in panel c) indicates Ekman heat flux anomaly differences significant at the 95% confidence level using a

two-sided Welch's t-test. Vectors in panel c are significant at the 95% confidence level. Note the color bar range and reference vector magnitude are smaller in panel c.

Fig. 8. Partial regression maps of wintertime turbulent heat flux anomalies regressed onto ENSO and Aleutian Low variability time series for the a-b) FC experiment and c-d) ERA5 Reanalysis from 1979-2019. Wintertime Niño-3.4 and the NPI index are defined as the independent predictor variables for the turbulent heat flux anomalies. Units are Wm^{-2} per unit standard deviation of the respective time series. The NPI index is multiplied by –1.0, as +Niño-3.4 and –NPI are associated with a deeper Aleutian Low.

Fig. 9. Similar to Fig. 6, except for wintertime precipitation rate. Units are mm day^{-1}. Stippling in panels d-e indicates precipitation anomaly differences significant at the 95% confidence level using a two-sided Welch's t-test.

Fig. 10. Similar to Fig. 8, except for wintertime precipitation rate (shading) and 500 hPa geopotential height (contours) anomalies from 1948-2020. The precipitation dataset is the NOAA PRECipitation RECONstruction, and geopotential heights are obtained from NCEP/NCAR Reanalysis. Precipitation units are mm day^{-1} per unit standard deviation of the respective time series. Geopotential height anomaly contours begin at +/– 4 meters and increase in 4 meter intervals.

Fig. 11. Similar to Fig. 6, except wintertime anomalous 200 hPa velocity divergence (shading) and anomalous 200 hPa velocity stream function (contours). Divergence units are 10^{-6} s^{-1} and stream function units are 10^{6} m^{2} s^{-1}. Positive (negative) divergence anomalies represent anomalous divergence (convergence).

Fig. 12. Similar to Fig. 6, except for wintertime 200 hPa zonal wind anomaly (shaded) and the overlaid contours for all panels are the wintertime 200 hPa zonal wind climatology from FC. Units are ms^{-1}. Note that the MD and MD_{EqPac} 200 hPa zonal wind climatologies are similar to FC, but FC is used for all for simplicity. Contour intervals for the climatology begin at +20 ms^{-1} and increase in amplitude in 10 ms^{-1} intervals. Stippling in panels d-e indicates zonal wind anomaly differences significant at the 95% confidence level using a two-sided Welch's t-test.

Tables

Table 1. Summary of each CESM1-CAM4 experiment setup, the sources of Aleutian Low variability in each experiment, and the processes that can drive the SST response to Aleutian Low variability. All experiments include dynamic atmosphere and ocean models, as well as land and sea ice models. All experiments include unconstrained buoyancy (heat and freshwater) fluxes.

Experiment	**Experiment Setup**	**Sources of Aleutian Low Variability**	**Processes that can drive the North Pacific SST response to Aleutian Low variability**
Mechanically decoupled (MD)	Global Ocean forced by climatological wind stresses	Internal atmospheric dynamics Non-ENSO SST variability	Non-ENSO air-sea heat fluxes
Mechanically decoupled equatorial Pacific (MD_{EqPac})	Equatorial Pacific Ocean forced by climatological wind stresses; remaining ocean grid points are fully coupled	Internal atmospheric dynamics Non-ENSO SST variability	Non-ENSO anomalous wind stress driven ocean dynamics Non-ENSO air-sea heat fluxes
Fully coupled (FC)	Fully coupled globally	Internal atmospheric dynamics Non-ENSO SST variability ENSO	Anomalous wind stress driven ocean dynamics Air-sea heat fluxes (*non-ENSO and ENSO forced*)

Table 2. Event count for anomalously strong (–NPI) and weak (+NPI) wintertime Aleutian low years. For the MD experiment, the event count in parenthesized italics is from a different 300-yr window not used in this analysis to show the low sensitivity of the sample size to the 300-yr window chosen for this experiment. Both MD_{EqPac} and FC are only 300 years total, so a similar sensitivity test is not performed.

Experiment	**–NPI** *+PDO-like SST response*	**+NPI** *–PDO-like SST response*
MD	37 *(43)*	34 *(38)*
MD_{EqPac}	37	44
FC	60	56

Figures

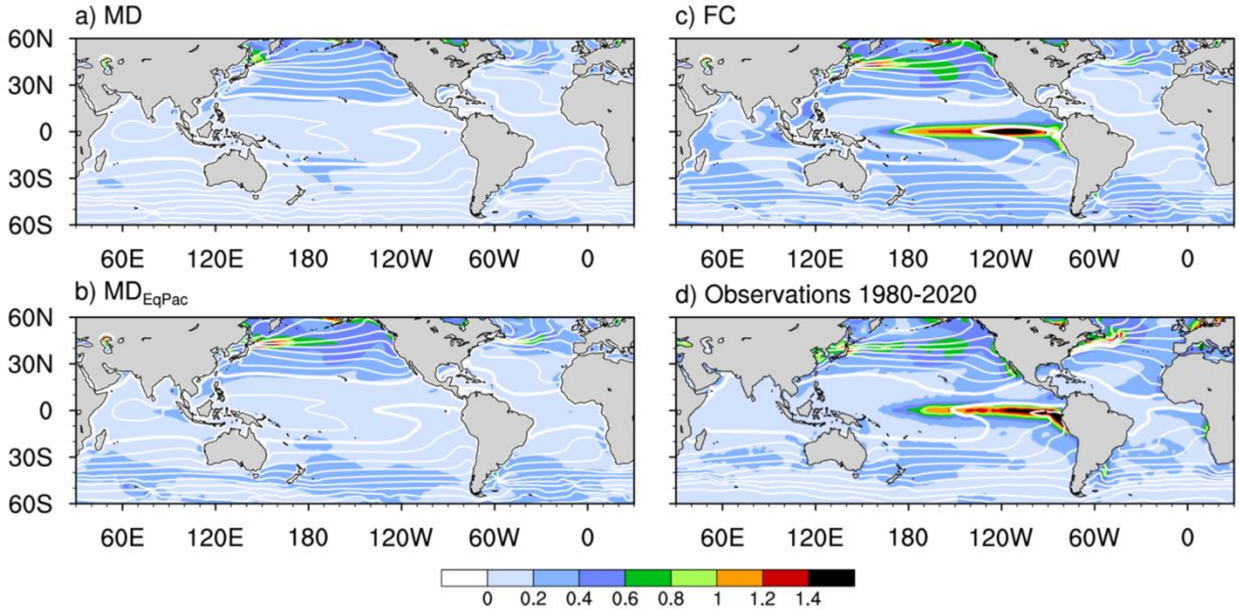

Fig. 1. Annual mean SST climatology (white contours) and monthly SST anomaly variance (shading) for experiments a) MD, b) MD_{EqPac}, c) FC, and d) observations from HadISST. Observations are taken from years 1980-2020 to roughly represent the year 2000 time period (model experiments are run with year 2000 forcing). The SST climatology contours are in 3°C intervals and the 27°C isotherm is in bold. SST variance is in units $(°C)^2$.

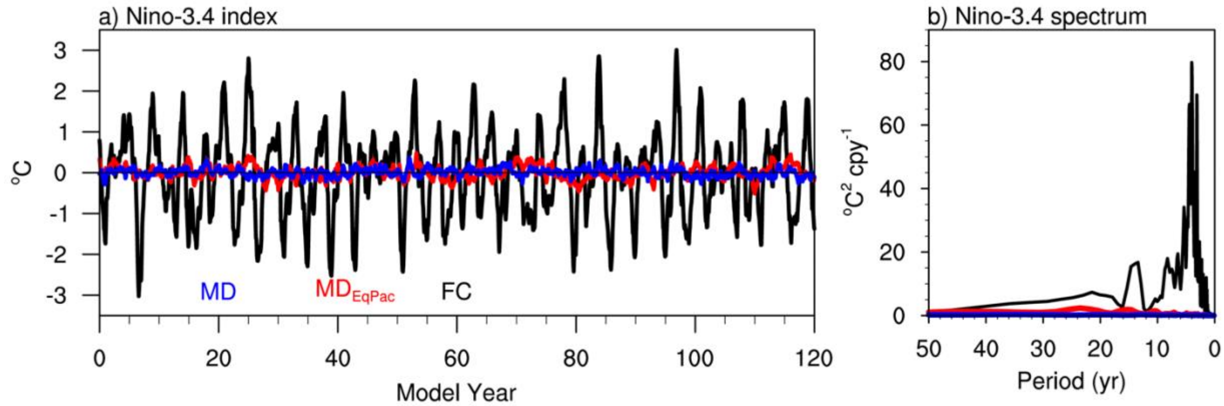

Fig. 2. ENSO variability in each experiment as estimated by the monthly Niño-3.4 SST anomaly index, defined as the area-averaged SST anomaly over 5°S-5°N, 170°W-120°W. a) Niño-3.4 SST anomaly index for 120 consecutive years from experiments for the MD, MD_{EqPac}, and FC Experiments. b) Niño-3.4 spectrum for each experiment, computed over the full 300 years of model data.

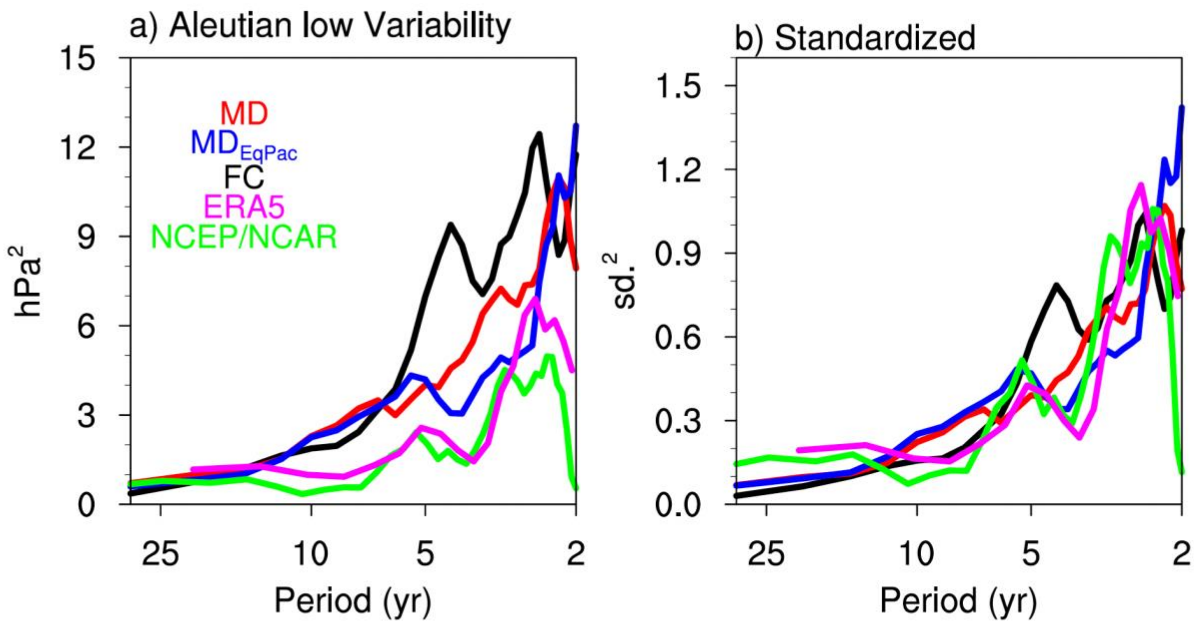

Fig. 3. a) Variance preserving power spectra of boreal wintertime Aleutian Low variability for the MD, MD$_{EqPac}$, and FC experiments and reanalysis products. Boreal winter Aleutian low variability is estimated using the NDJFM-averaged North Pacific Index (NPI), defined as the area-averaged sea level pressure anomalies over 30°N-65°N, 160°E-140°W. A 5-point Daniell smoothing is applied to the spectral estimates. For each of the model experiments, the NPI is divided into 60-yr non-overlapping windows, the spectrum is computed for each window, and the average spectra over the windows is displayed. b) Same as a) except each NPI time series is standardized by its own standard deviation prior to spectral analysis.

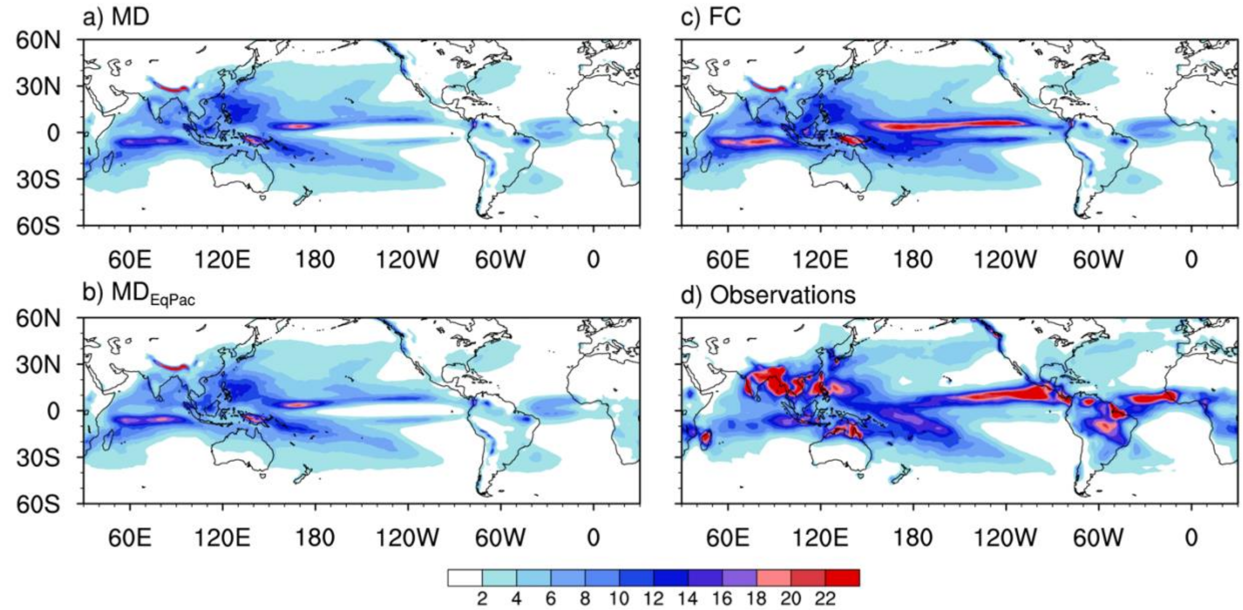

Fig. 4. Monthly precipitation anomaly variance for a) MD, b) MD$_{EqPac}$, c) FC, CESM1-CAM4 experiments and d) observations from GPCP 1979-2020. Units are (mm day^{-1})^2.

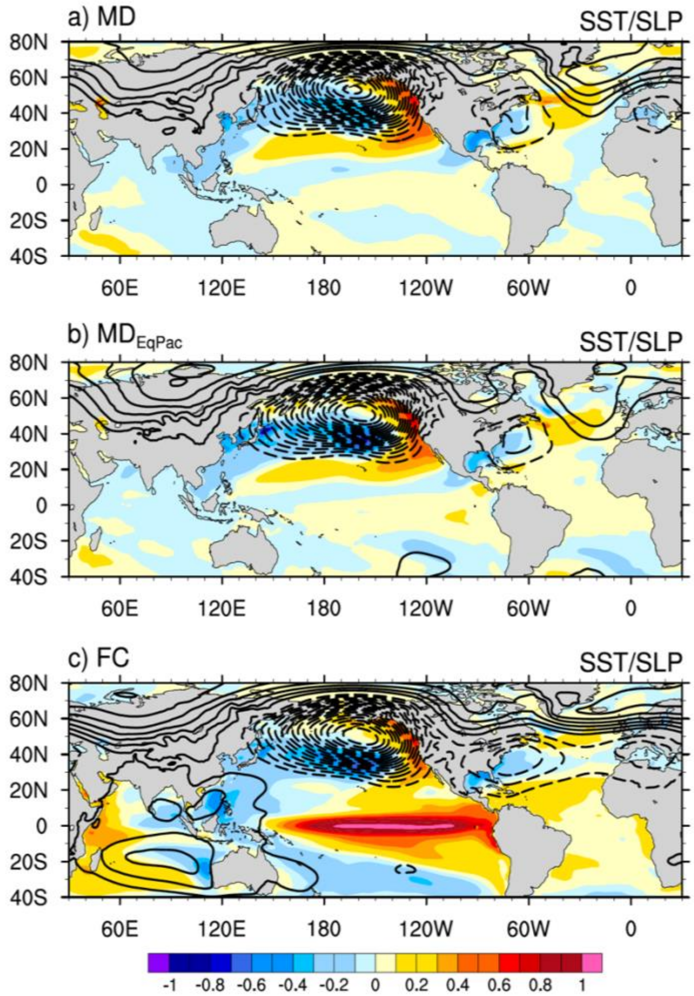

Fig. 5. Composite averaged wintertime SST (shading) and sea level pressure (SLP; black contours) anomalies associated with Aleutian Low variability for the MD, MD_{EqPac}, and FC experiments. Events are defined as meeting or exceeding +/– one standard deviation of the wintertime NPI. Composites are displayed as [–NPI - (+NPI)] / 2 to reflect the spatial pattern and typical amplitude of a deepened Aleutian Low and the +PDO-like SST anomaly response. SLP contour intervals begin at +/– 0.5 hPa and increase in amplitude in 0.5 hPa intervals. Dashed contours indicate negative SLP anomalies. SST anomalies are in °C. Wintertime months are defined as NDJFM.

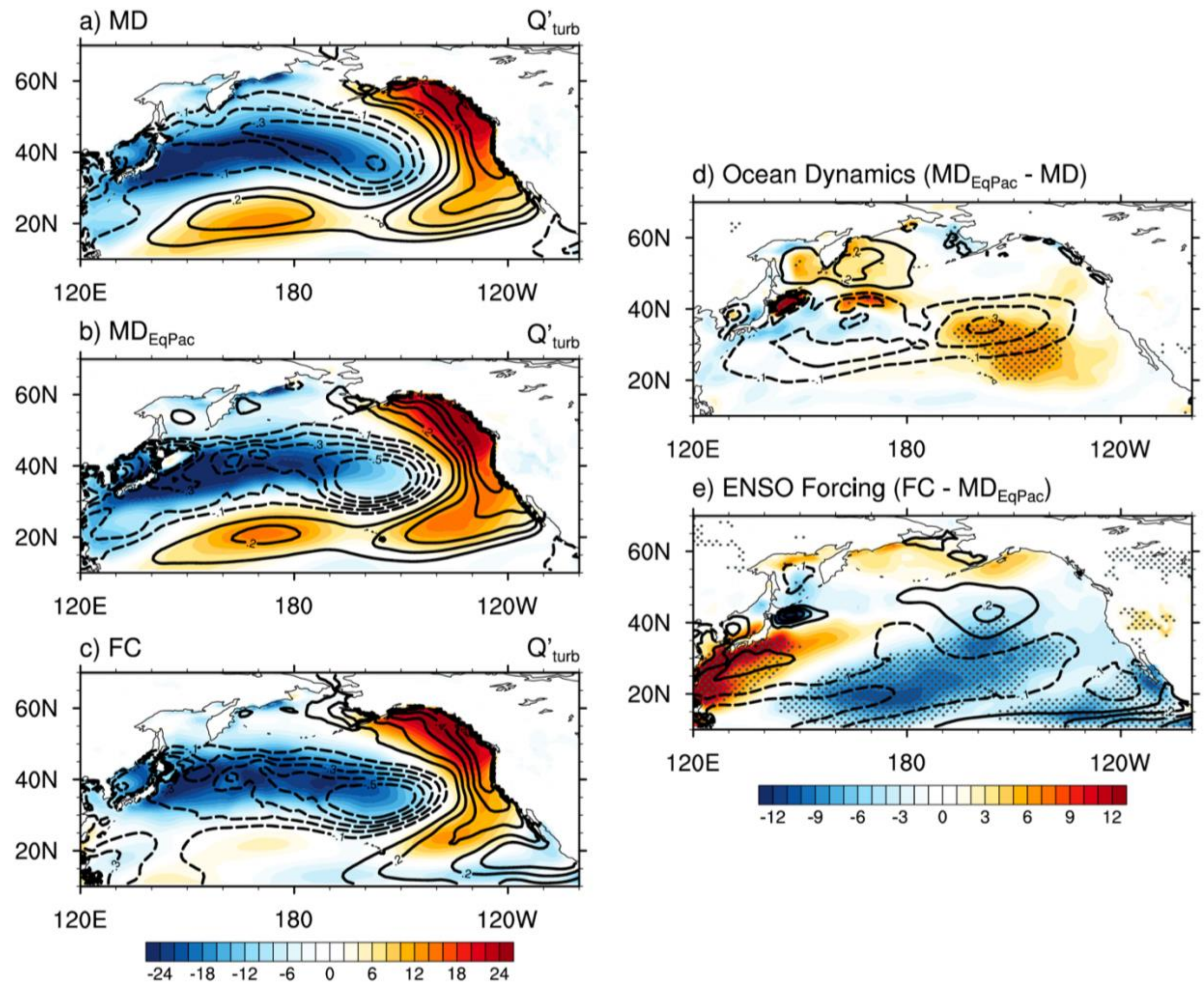

Fig. 6. North Pacific composite average wintertime turbulent heat flux (shading) and SST (contours) anomalies associated with Aleutian Low variability for a-c) each model experiment and d-e) their differences. Events are defined as meeting or exceeding +/– one standard deviation of the wintertime NPI. Composites are displayed as [–NPI - (+NPI)] / 2 to reflect the spatial pattern and typical amplitude of anomalies associated with a deepened Aleutian Low. Turbulent heat fluxes are calculated as the sum of the sensible and latent heat flux anomalies. The sign convention is a positive (negative) heat flux is into the ocean, or a warming (cooling) and units are Wm^{-2}. SST anomaly contour intervals begin at +/– 0.1 °C and increase in amplitude in 0.1°C intervals. Negative contours indicate negative SST anomalies. Wintertime months are defined as

NDJFM. Stippling in panels d-e indicates turbulent heat flux anomaly differences significant at the 95% confidence level using a two-sided Welch's t-test.

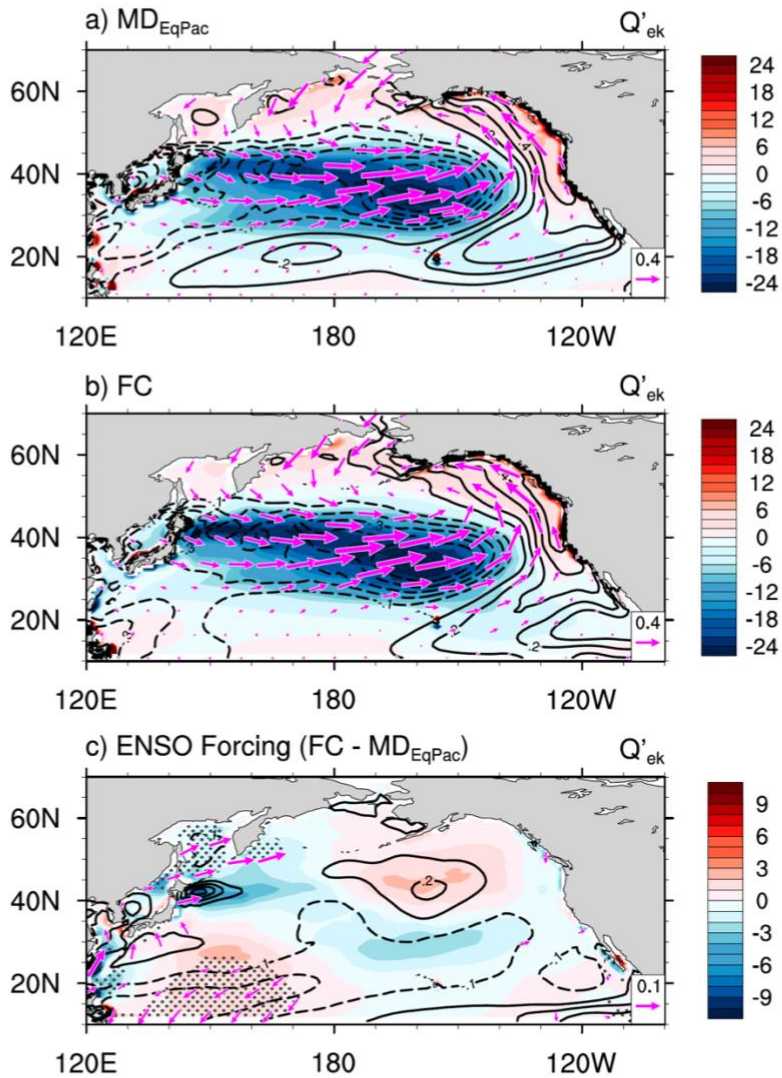

Fig. 7. Similar to Fig. 6b,c,e, except for wintertime anomalous wind stress driven Ekman heat flux (shading) and SST (contours) anomalies. Ekman heat flux anomaly units are Wm^{-2}. SST anomaly contour intervals begin at +/– 0.1 °C and increase in amplitude in 0.1°C intervals. Magenta vectors are the composite wind stress anomaly in units Nm^{-2}. Stippling in panel c) indicates Ekman heat flux anomaly differences significant at the 95% confidence level using a two-sided Welch's t-test. Vectors in panel c are significant at the 95% confidence level. Note the color bar range and reference vector magnitude are smaller in panel c.

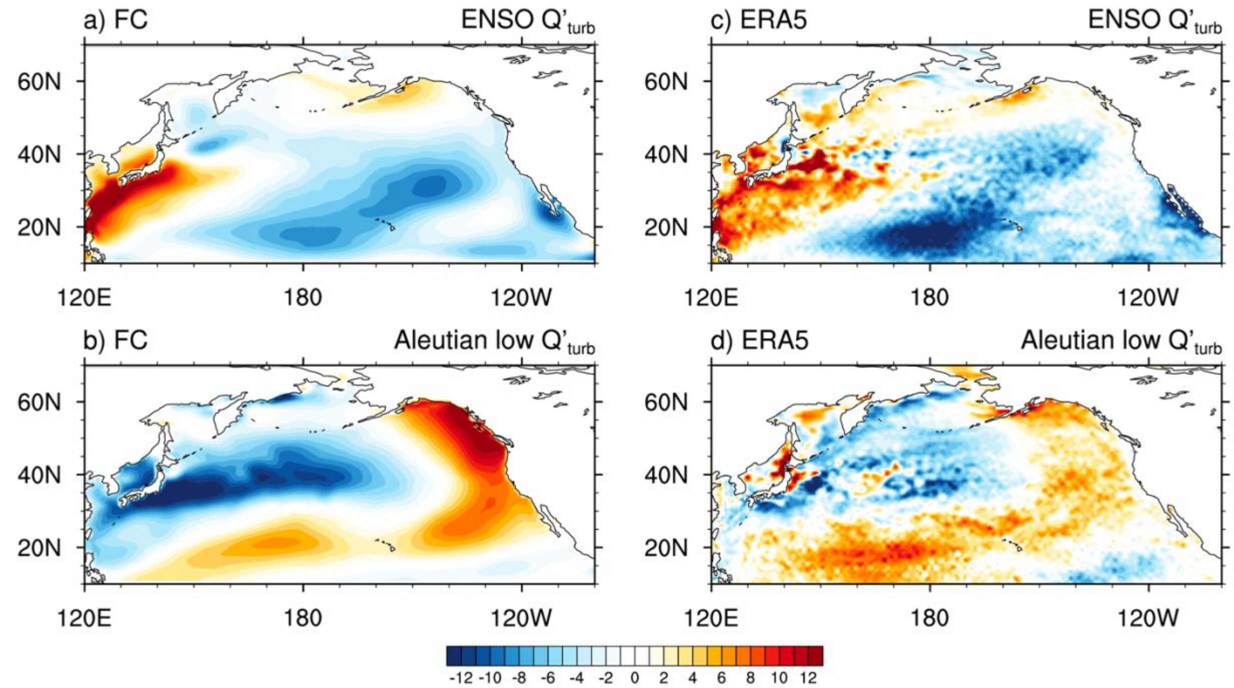

Fig. 8. Partial regression maps of wintertime turbulent heat flux anomalies regressed onto ENSO and Aleutian Low variability time series for the a-b) FC experiment and c-d) ERA5 Reanalysis from 1979-2019. Wintertime Niño-3.4 and the NPI index are defined as the independent predictor variables for the turbulent heat flux anomalies. Units are Wm^{-2} per unit standard deviation of the respective time series. The NPI index is multiplied by –1.0, as +Niño-3.4 and –NPI are associated with a deeper Aleutian Low.

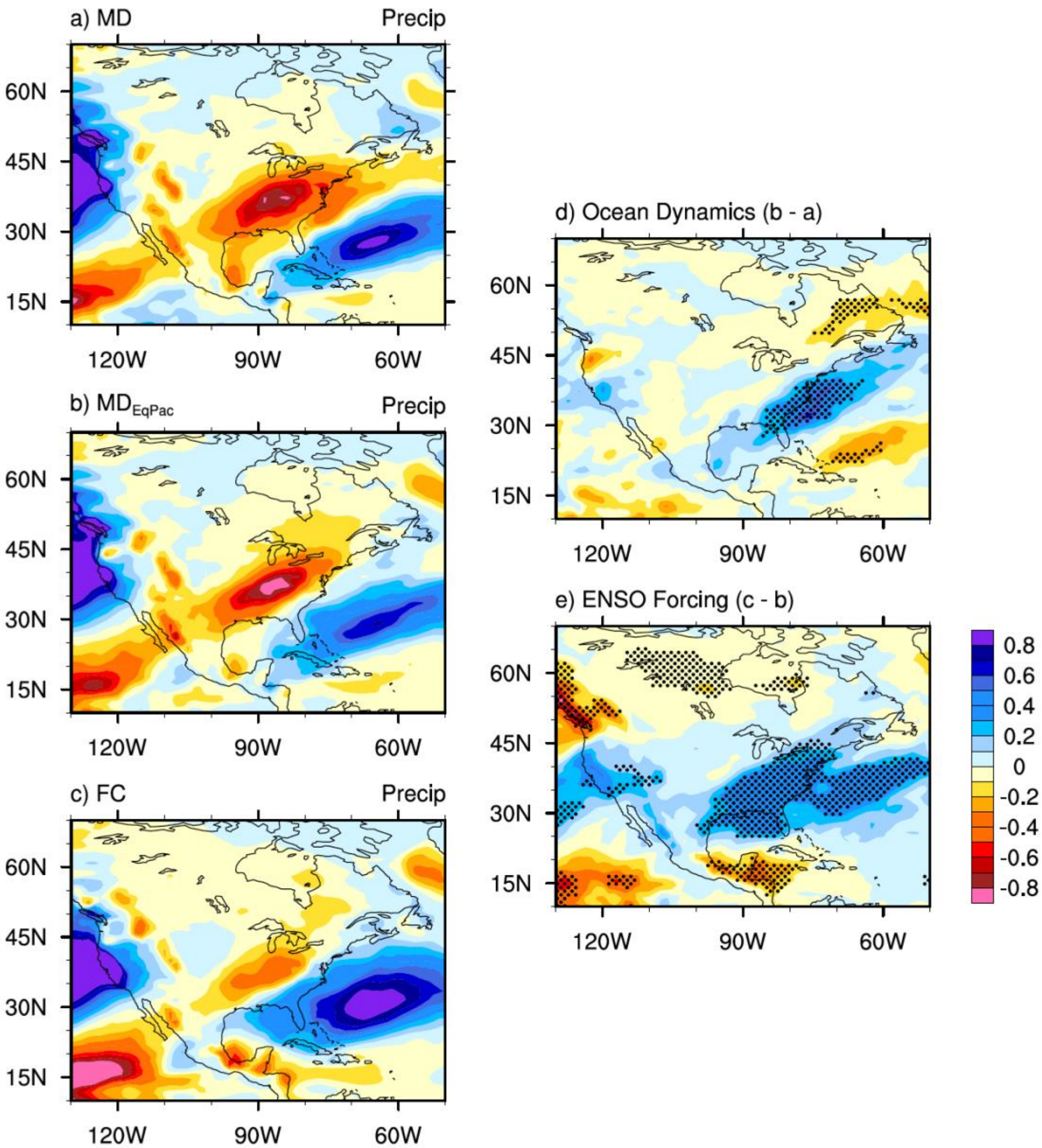

Fig. 9. Similar to Fig. 6, except for wintertime precipitation rate. Units are mm day^{-1}. Stippling in panels d-e indicates precipitation anomaly differences significant at the 95% confidence level using a two-sided Welch's t-test.

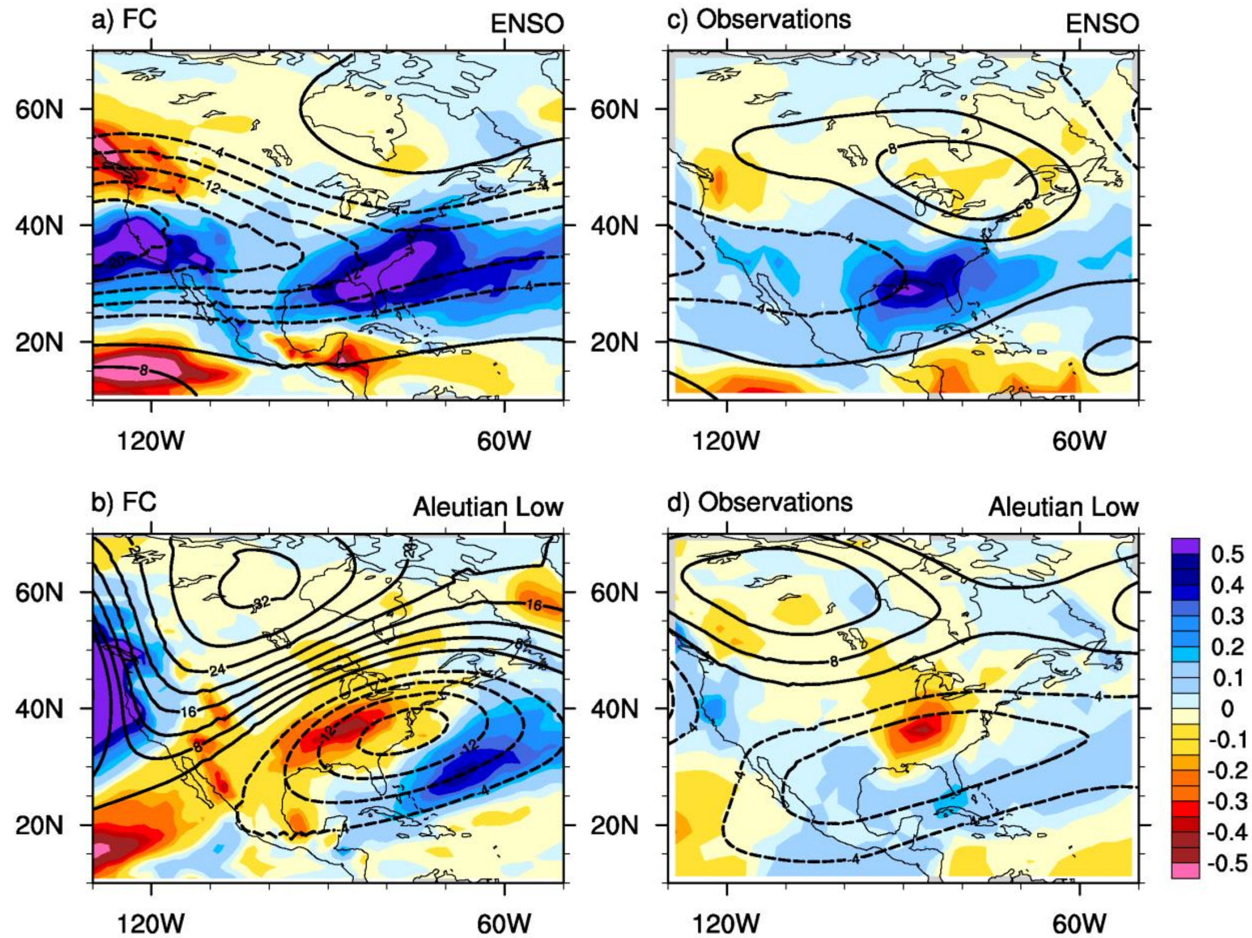

Fig. 10. Similar to Fig. 8, except for wintertime precipitation rate (shading) and 500 hPa geopotential height (contours) anomalies from 1948-2020. The precipitation dataset is the NOAA PRECipitation REConstruction, and geopotential heights are obtained from NCEP/NCAR Reanalysis. Precipitation units are mm day^{-1} per unit standard deviation of the respective time series. Geopotential height anomaly contours begin at +/– 4 meters and increase in 4 meter intervals.

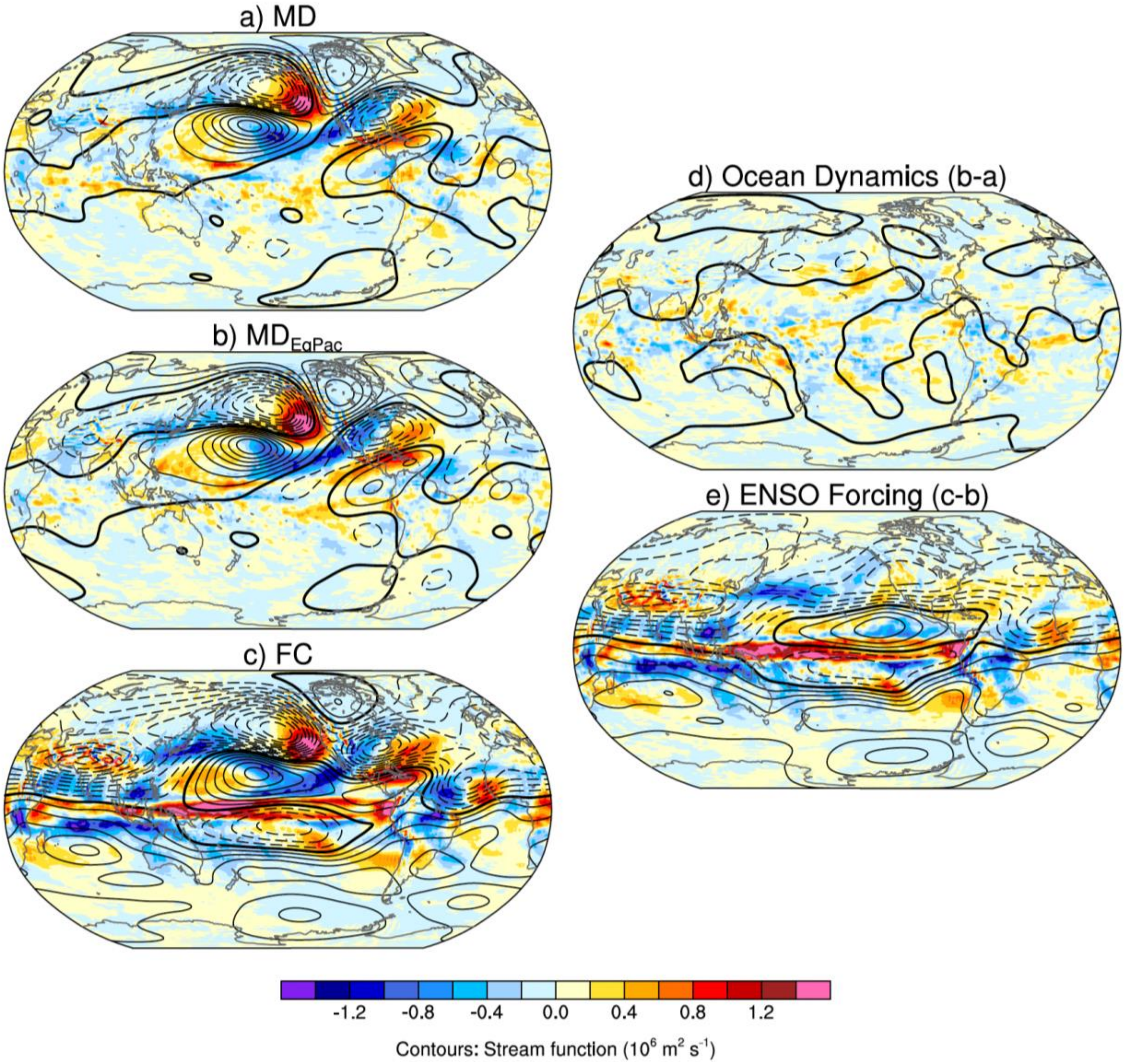

Fig. 11. Similar to Fig. 6, except wintertime anomalous 200 hPa velocity divergence (shading) and anomalous 200 hPa velocity stream function (contours). Divergence units are 10^{-6} s^{-1} and stream function units are 10^{6} m^{2} s^{-1}. Positive (negative) divergence anomalies represent anomalous divergence (convergence).

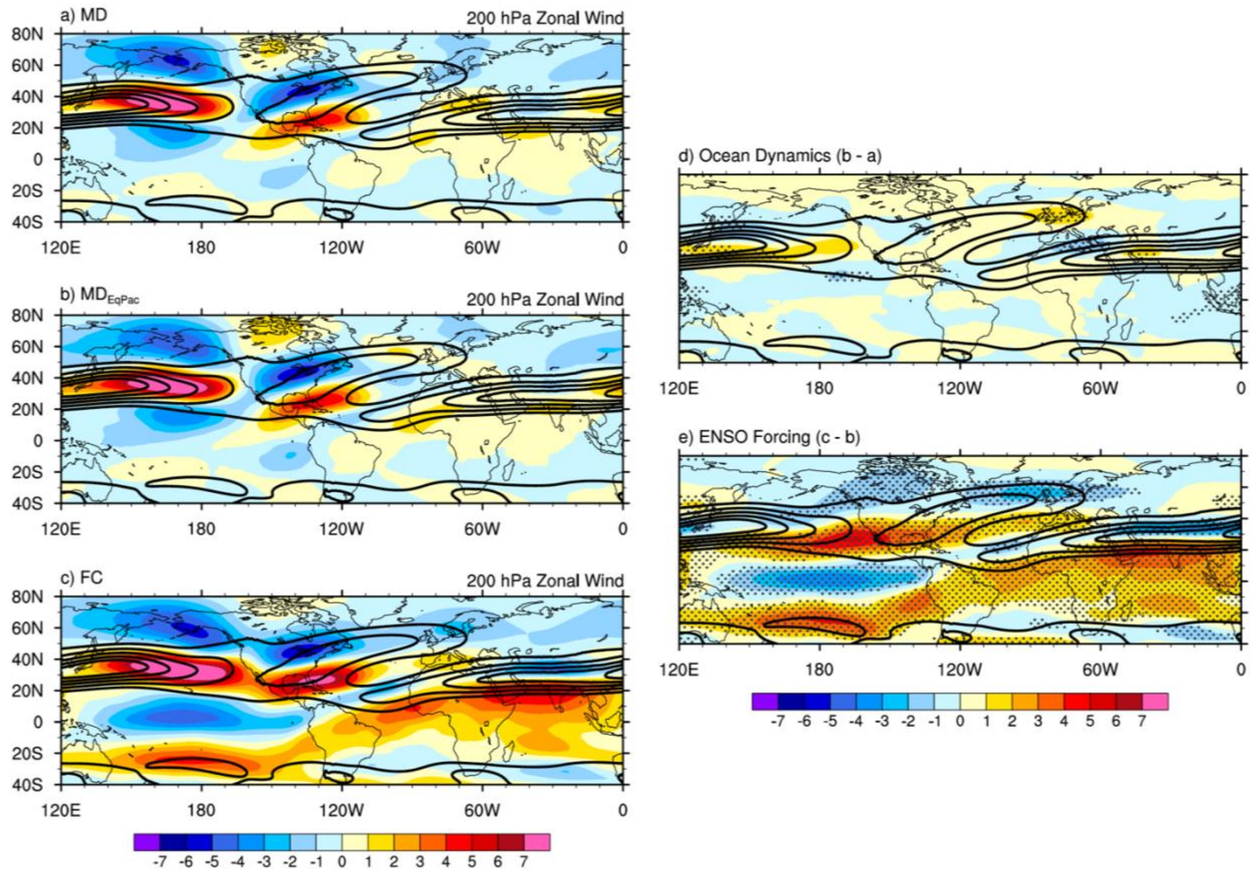

Fig. 12. Similar to Fig. 6, except for wintertime 200 hPa zonal wind anomaly (shaded) and the overlaid contours for all panels are the wintertime 200 hPa zonal wind climatology from FC. Units are ms^{-1}. Note that the MD and MD_{EqPac} 200 hPa zonal wind climatologies are similar to FC, but FC is used for all for simplicity. Contour intervals for the climatology begin at +20 ms^{-1} and increase in amplitude in 10 ms^{-1} intervals. Stippling in panels d-e indicates zonal wind anomaly differences significant at the 95% confidence level using a two-sided Welch's t-test.